PCCP

Polytelluride compounds containing distorted nets of tellurium

Rhonda Patschke and Mercouri G. Kanatzidis

Department of Chemistry, Michigan State University, East Lansing, MI 48864, USA

Received 31st January 2002, Accepted 18th April 2002
First published as an Advance Article on the web 17th June 2002

The propensity of solid state polytelluride compounds to form structures with extended square nets of tellurium and the physicochemical properties of these nets is discussed in view of recent results showing that these square nets of tellurium are in fact average structures. The real structures are strongly modulated, giving rise to patterns within these nets that involve polytelluride oligomers. The patterns are dictated by the average electron-count on the tellurium atoms and often, sophisticated crystallographic techniques (electron diffraction, superstructure, and super spacegroup approaches) are required to elucidate them. In this account we discuss the structural peculiarities observed in $KCuCeTe_4$, $RbCuCeTe_4$, $Na_{0.8}Ag_{1.2}CeTe_4$, $K_{2.5}Ag_{4.5}Ce_2Te_9$, $K_{2.5}Ag_{4.5}La_2Te_9$, $Cu_{0.66}EuTe_2$, KCu_2EuTe_4, $Na_{0.2}Ag_{2.8}EuTe_4$, and $K_{0.65}Ag_2Eu_{1.35}Te_4$.

Introduction

One important difference between Te_x^{2-} and Q_x^{2-} (Q = S, Se) ions is the greater tendency for the former to associate through weak Te–Te bonding interactions because of the more diffuse nature of its orbitals.[1–3] This fact makes polytelluride phases distinct in their structure and properties. A noteworthy structural motif in polytellurides is the formation of infinite two-dimensional square-net sheets. This particular arrangement and its consequences in the observed properties are the subject of this article. Tellurium square nets were thought to be rare until recently. The known compounds included $LnTe_2$, Ln_2Te_5, and $LnTe_3$,[4] and some actinide analogs. In the past decade however many new, more complex phases were discovered as for example $K_{0.33}Ba_{0.67}AgTe_2$,[3] Cs_3Te_{22},[5] $CsTh_2Te_6$,[6] and ALn_3Te_8 (A = Cs, Rb, K; Ln = Ce , Nd).[1] With the aid of the molten alkali metal/polytelluride flux method,[7] we identified a new family of complex phases containing Te nets. Examples include $KCuCeTe_4$,[8] $RbCuCeTe_4$,[9] $Na_{0.8}Ag_{1.2}CeTe_4$,[9] $K_{2.5}Ag_{4.5}Ce_2Te_9$,[9] $K_{2.5}Ag_{4.5}La_2Te_9$,[9] $Cu_{0.66}EuTe_2$,[10] KCu_2EuTe_4,[10] $Na_{0.2}Ag_{2.8}EuTe_4$,[10] and $K_{0.65}Ag_2Eu_{1.35}Te_4$.[9] Although many of these possess new structure types, they still retain features of the known binary rare earth tellurides (*e.g.* $NdTe_3$[11]-type) which at first glance appear to possess perfectly square Te nets. Careful crystallographic and physicochemical examination, however, combined with electron diffraction studies show that most of these Te nets are in fact modulated. This characteristic is a consequence of mixed valency on the Te sites in the net. It can be a real challenge to understand the properties of these solids on the basis of the observed average crystal structures.

Based on conventional bonding theory, an array of Te atoms arranged in an ideal square net is expected to be inherently unstable unless the formal oxidation state of each Te atom is −2, *i.e.* 8 electrons per Te atom. In this case there are no Te–Te interactions. A good example of this is found in NaCuTe.[12] Anything less than a −2 charge will induce strong attractive Te–Te bonding interactions and the formation of Te_x^{n-} species, *i.e.* polytellurides. This situation is exactly the two-dimensional equivalent of an ideal linear chain of hydrogen atoms that is strongly susceptible to a Peierls distortion and the formation of dimers. In both cases the total energy of the ideal system is higher than that of the distorted system and it is this energy difference that provides the powerful driving force for the distortion to occur. It is important to realize that from an ideal square net, the distortion pattern will vary depending on the degree of electron deficiency, *i.e.* how far away it is from the maximum number of 8 electrons per Te atom. Thus depending on electron-count, these nets can have different electron fillings which can lead to various instabilities and structural distortions within them.[13] Generally, such distortions are manifested through the formation of a superstructure with respect to the ideal square net. One way of describing these distortions is as "localized" charge density waves (CDWs).[14] Determining the nature of these distortions is important because the chemical, physical, and electronic properties of these compounds are largely decided by these square nets, and by their interaction with the remaining part of the structure.

Papoian and Hoffmann have discussed homo-atomic interactions between main-group elements, including tellurium, recently in an excellent review.[15] They focus on a broad set of elements and structures and, in connection to tellurides, they discuss predominantly rare-earth and actinide binary polytelluride compounds. It is the purpose of this paper to focus on more complex examples of compounds with square Te nets and review recent results. We will discuss the proclivity of square Te nets for superstructure formation, the reasons for this, and new examples of compounds that exhibit such phenomena. We will also emphasize the dangers in determining only the average crystal structure of such compounds and the inadequacies of these structures in explaining the observed properties.

Results and discussion

The archetypal compounds with square Te nets are the binary $LnTe_2$, Ln_2Te_5, and $LnTe_3$ (Ln = La, Ce, Nd, Sm, Gd, Tb, Dy, Ho, Er, Tm) systems which have been known for many decades. The original crystallographic analysis on these compounds indicated Te layers in the shape of more or less perfect square nets with Te–Te separations of 3.08 Å.[11] Despite the fact that these longer than normal bond distances suggest something unusual is going on in these compounds, an in-depth look at their structure was not taken until recently. Transmission electron microscopy (TEM) and, more specifically, electron diffraction studies on these layered rare-earth tritellurides, LnTe$_3$, have since identified superlattice reflections indicating the presence of incommensurate distortions, consistent with periodic atomic displacements in the square Te sheets. The resulting charge density waves (CDWs) are stable under the volume decreases obtained by substituting the heavier rare earths, and thus the distortion wave vector scales, with the lattice parameters across the rare-earth series.[16] The superlattice wave vector can sometimes be predicted to correspond to the maximal Fermi-surface nesting wave vector determined from extended Hückel tight-binding band structure calculations.[17] Despite the very simple but universal chalcogen sheet band structure, these rare-earth polychalcogenides represent a family of CDW hosts in which a variety of structural distortions occur with variation of chalcogen type and stoichiometry.

The ideal square net arrangement of Te atoms with an average formal oxidation state of <-2 will result in an electronic band structure where the Fermi level crosses over one or more bands. This situation defines a metallic system. Such a configuration is in fact unstable in principle and clues for its instability can be found in the observed average Te–Te bonding distances of 3.0–3.1 Å, which are much longer than the normal covalent Te–Te distances of classical polytellurides Te_n^{2-} (~2.8 Å). These long distances do not represent any type of understood or known bonding situation in tellurides. To form normal Te–Te bonds of ~2.8 Å, distortions are needed in the net in which Te atoms move away from their ideal positions. These displacements result in both long (~3.4 Å) and short (~2.8 Å) distances. This converts a situation of all weak interactions in the ideal square net to a situation of some strong and some weak interactions in the distorted net. In other words, the energy lowering and stabilization obtained from the 2.8 Å bonds greatly outweighs any destabilization deriving from breaking the already very weak 3.0 Å separations. Therefore, arguably a distortion in these cases is inevitable. Fig. 1 schematically shows how the distortion described above generates a modulation of the Te–Te separations that changes the putative metallic system to actual semiconducting or semimetallic systems, both of which lie lower in energy. The filled states, removed from the neighborhood of the Fermi level (E_F), are pushed lower in energy, whereas the corresponding empty states are pushed higher. Exactly how this happens depends on the position of E_F or, stated differently, the average oxidation state of Te^{n-} ions in the square net. Some possible patterns (or CDWs) derived from a modulation in an ideal square net are shown in Scheme 1. The bold lines in the scheme indicate normal Te–Te bonding of ~2.8 Å, while the dotted lines represent very weak bonding of >3.1 Å. The following discussion will focus on $K_{0.33}Ba_{0.67}AgTe_2$,[3] $ACuCeTe_4$ (A = K, Rb),[8,9] $Na_{0.8}Ag_{1.2}CeTe_4$,[8] $K_{2.5}Ag_{4.5}Ln_2Te_9$ (Ln = La, Ce),[9] $Cu_{0.66}EuTe_2$,[10] KCu_2EuTe_4,[10] and $Na_{0.2}Ag_{2.8}EuTe_4$.[10] These compounds possess structural modulations, often incommensurate, that can be attributed to differences in Te–Te bonding and vary depending on the compound. In several cases, the superstructure has been resolved and the distortions found in the nets have been both surprising and eye opening.

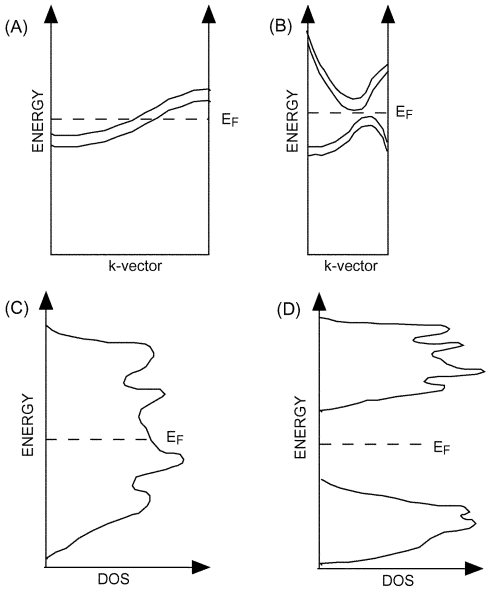

Fig. 1 Schematic representation of a possible band structure of: (A) an ideal square net showing metallic character; (B) a Te net after distortion showing the opening of a band gap at the Fermi level, E_F; (C) DOS diagram of an ideal square net; (D) DOS diagram of a distorted net showing opening of a band gap at E_F. This is a generic cartoon only and is not meant to approximate how such a band dispersion will occur.

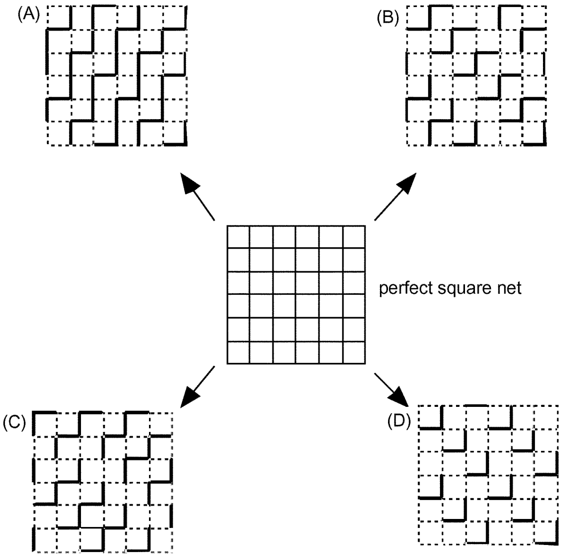

Scheme 1

$K_{0.33}Ba_{0.67}AgTe_2$. The first quaternary compound to exhibit square Te nets was $K_{0.33}Ba_{0.67}AgTe_2$.[3] The originally determined crystal structure was tetragonal and unmistakably showed a perfect square net with Te–Te distances of 3.0 Å. A perspective view of the layered tetragonal crystal structure (space group $I4/mmm$ with $a = 4.624(2)$ Å, $c = 23.326(4)$ Å) is shown in Fig. 2. This layered motif features alternating square Te sheets and [AgTe] slabs. The nets are sandwiched between two monolayers of K/Ba cations. If a formal oxidation state of -2 and $+1$ were assigned to the Te and Ag atoms in the anti-PbO [AgTe] slab, respectively, then a $-2/3$ charge corresponds to each Te atom in the square net. The closest Te–Te distance in the net is 3.269(2) Å, too long for a covalent bond, but shorter than a van der Waals contact. While it is predicted that a perfect square net with $Te^{-0.67}$ atoms should have metallic properties, the experimental data showed semiconducting behavior raising the suspicion that something was amiss in the crystal structure. A substantial clue was found in the thermal ellipsoids of the Te sites in the net, which showed distinct flattening (a "pancake" shape) in the *ab*-plane, *i.e.* the plane of the Te net. The absence of this ellipsoid asymmetry in the other atomic sites (*e.g.* Ag, K/Ba *etc.*) alerted us to the possibility of a superstructure in these nets. Indeed, electron diffraction experiments on very thin platelets revealed the presence of an incommensurate orthorhombic superstructure with $a(\text{super}) = 2.84a$, $b(\text{super}) = b$, and $c(\text{super}) = c$. These results strongly suggested electron *locali-*

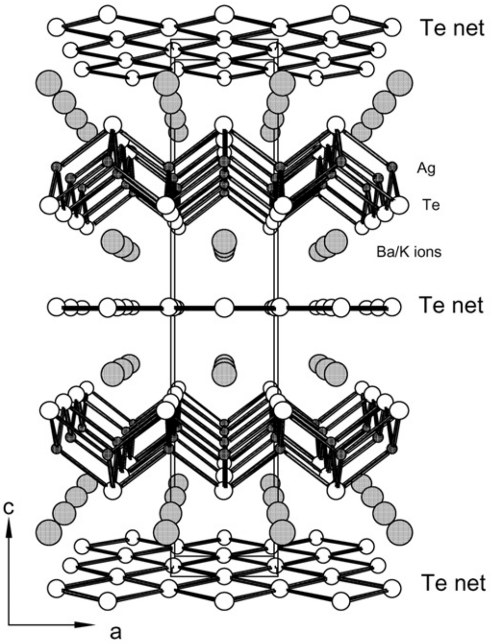

Fig. 2 The ideal crystal structure of $K_{0.33}Ba_{0.67}AgTe_2$.

zation in the form of a charge density wave (CDW). Since the formal negative charge per Te atom is −0.67, it is reasonable to expect that a CDW may result as discrete Te_3^{2-} units. Extended-Hückel calculations confirmed that this distortion is a charge density wave.

Although electron diffraction experiments showed clearly evidence for a modulation, the information obtained was limited to two dimensions (*ab*-plane). In order to get full three-dimensional structural information, we grew larger crystals and performed a full single crystal X-ray analysis that unequivocally solved the incommensurate superstructure.[18] The modulated structure was determined within a (3 + 1)D higher dimension formalism with surprising results. The phase was found to possess monoclinic symmetry with an additional modulation along the *c*-direction. Superspace group was $P2_1(R0\gamma)$ with the following lattice parameters: $a = 4.6441(10)$ Å, $b = 4.6292(12)$ Å, $c = 23.765(9)$ Å, and $\beta = 101.28(2)°$ with $q = 0.3248(6)a^* - 0.071(8)c^*$. This type of analysis identified not only the presence of the predicted V-shaped Te_3^{2-} trimer anions, but also revealed additional significant structural features which could not have been detected by the techniques used earlier. These features include the existence of the rare W-shaped Te5 pentamer anions, see Fig. 3.[18]

In agreement with the fact that the V-pattern domains are slightly larger than the W-pattern domains in the modulated structure, the band structure calculations indicate that both the V- and W-pattern distortions are stabilized in nature and that the V-pattern distortion is more stable. In addition, they reveal that although the nesting vectors of the Fermi surface of the undistorted square-net Te layers are consistent with the observed V- and W-patterns, the stabilization energy is dominated by low lying band levels. In other words, the energy gain is derived not only from what happens near the Fermi level, but also from the lowering of orbital energies well below it. It is worth noticing that not only is the Te5 structural motif unprecedented, but also that two different Te_x^{n-} anions occur in the same plane. This is a remarkable discovery and implies that the factors giving rise to the particular aperiodic structures in Te-square nets are subtle, and begs for the structural determination of additional such structures, as for example those presented below.

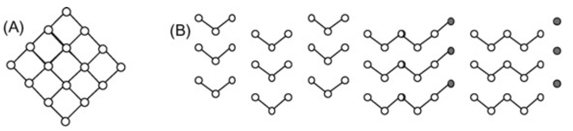

Fig. 3 Striking difference between (A) the structure of the square Te-net determined by conventional crystallography (average tetragonal structure) which predicts a metallic compound and (B) the structure of the incommensurately modulated Te-net determined by higher dimensional crystallography. Two motifs are observed: Te groups with a "V" shape and Te groups with a "W" shape. Occasionally, as the motif changes from V to W, the lone Te atom (black dots) found between two W motifs is at a distance slightly shorter than 3.1 Å of a W motif (one such example is observed in the figure). This structure explains the narrow band-gap semiconductor behavior of this compound.

$A_xM_{(2-x)}CeTe_4$. A fascinating group of compounds containing superstructures is defined by $A_xM_{(2-x)}CeTe_4$ (A = Na, K, Rb; M = Cu, Ag). $KCuCeTe_4$ and $RbCuCeTe_4$ exhibit a two-dimensional structure composed of two "distinct" layers, $[CuTe]^-$ and $[CeTe_3]$, see Fig. 4. Because each layer is known to exist independently, $KCuCeTe_4$ can be regarded as an intergrowth compound and a more descriptive formula would be $K^+[CuTe]^-[CeTe_3]$. The $[CuTe]^-$ layer is isostructural to the [AgTe] layer of $K_{0.33}Ba_{0.67}AgTe_2$. The $[CeTe_3]$ layer adopts the $NdTe_3$ structure type, has 9-coordinate Ce atoms, see Fig. 4B, and contains a square Te lattice net, see Fig. 4C. Within this net, all the Te–Te distances are equal at 3.14 Å, which is longer than the normal Te–Te bond of 2.8 Å but shorter than the van der Waals contact of 3.8–4.0 Å.

The Te net in the $[CeTe_3]$ layer of $KCuCeTe_4$ is fully occupied. However, the formal oxidation state of the Te atoms in this net is −0.5, indicating the possibility of a distortion within the Te net. This distortion should be different than that of $K_{0.33}Ba_{0.67}AgTe_2$ because of the smaller average charge per Te atom. Notice the $[CuTe]^-$ layer also has a square Te net; however, the −2 formal charge on each Te atom in this layer is not expected to lead to a distortion. Consequently, any observed superstructure must originate from the $[CeTe_3]$ part of the compound.

$Na_{0.8}Ag_{1.2}CeTe_4$ is isostructural to $KCuCeTe_4$. The non-stoichiometry in $Na_{0.8}Ag_{1.2}CeTe_4$ is due to a 20% mixed occu-

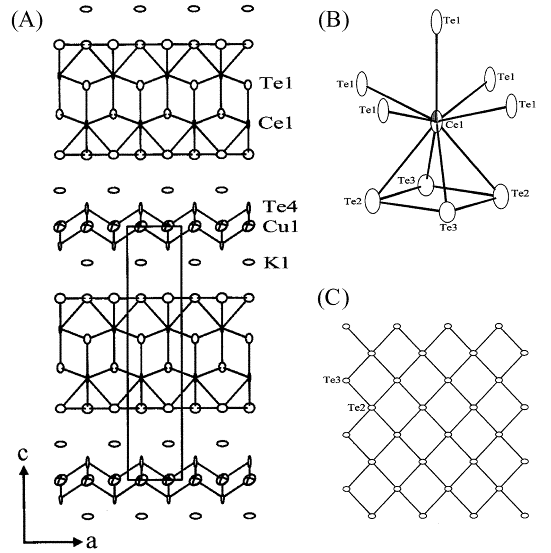

Fig. 4 (A) ORTEP representation of the extended structure of $KCuCeTe_4$ as seen down the *b*-axis (90% probability ellipsoids). The ellipsoids with solid black shading represent Ce, the crossed ellipsoids represent Cu, the large open ellipsoids represent K and Te. (B) The coordination environment around Ce in $KCuCeTe_4$. (C) A view perpendicular to the Te net portion of the $[CeTe_3]$ layer in $KCuCeTe_4$.

Table 1 Crystallographic data for $KCuCeTe_4$, $RbCuCeTe_4$, and $Na_{0.8}Ag_{1.2}CeTe_4$

	$KCuCeTe_4$	$RbCuCeTe_4$	$Na_{0.8}Ag_{1.2}CeTe_4$
Crystal habit, color	Plate, copper	Plate, copper	Plate, copper
Diffractometer	Rigaku AFC6S	Siemens SMART Platform CCD	Rigaku AFC6S
Radiation	Mo-Kα (0.71069 Å)	Mo-Kα (0.71073 Å)	Mo-Kα (0.71069 Å)
Crystal size/mm^3	$0.29 \times 0.29 \times 0.03$	$0.18 \times 0.31 \times 0.02$	$0.23 \times 0.23 \times 0.02$
Temperature/K	293	173	293
Crystal system	Orthorhombic	Orthorhombic	Orthorhombic
Space group	*Pmmn* (#59)	*Pmmn* (#59)	*Pmmn* (#59)
a/Å	4.436(1)	4.4330(9)	4.450(3)
b/Å	4.4499(9)	4.4697(9)	4.448(4)
c/Å	21.304(2)	21.951(4)	20.25(1)
V/$Å^3$	420.5(4)	434.95(15)	401.3(5)
Z	2	2	2
μ/mm^{-1}	22.02	26.219	22.69
Index ranges	$0 \leqslant h \leqslant 5$	$-5 \leqslant h \leqslant 0$	$0 \leqslant h \leqslant 5$
	$-5 \leqslant k \leqslant 5$	$-5 \leqslant k \leqslant 5$	$0 \leqslant k \leqslant 5$
	$-25 \leqslant l \leqslant 25$	$-28 \leqslant l \leqslant 28$	$-24 \leqslant l \leqslant 24$
$2\theta_{max}$/°	50	50	50
Seconds per frame	N/A	40	N/A
Total data	1701	2645	1837
Unique data	498	641	815
R(int)	0.065	0.156	0.032
No. parameters	30	30	28
Final R/Rw^a/%	6.36/5.76	N/A	7.20/9.20
Final $R1/wR2^b$/%	N/A	10.34/27.37	N/A
GOF	2.609	1.048	4.92

[a] $R = \sum(|F_o| - |F_c|)/\sum|F_o|$ $Rw = \{\sum[w(F_o - F_c)^2]/\sum[w(F_o)^2]\}^{1/2}$. [b] $R1 = \sum(|F_o| - |F_c|)/\sum|F_o|$ $wR2 = \{\sum[w(F_o{}^2 - F_c{}^2)^2]/\sum[w(F_o{}^2)^2]\}^{1/2}$.

pancy on the sodium site with silver. The crystallographic data, refinement details, fractional atomic coordinates, and isotropic and anisotropic temperature factors for all three compounds are given in Tables 1–3. In this case, too, the presence of an apparently ideal Te net cannot be readily accepted given the observed Te–Te distances and expected average oxidation states for the Te atoms. Instead a distortion or modulation should be suspected.

To probe for this modulation, electron diffraction studies were performed on $KCuCeTe_4$ and $Na_{0.8}Ag_{1.2}CeTe_4$ and a superstructure was revealed along the *ab* plane. The supercell reflections are very weak, and occur along both the a^* and b^* directions. Fig. 5A shows an electron diffraction pattern of the (hk0) zone of $KCuCeTe_4$ and a densitometric intensity scan obtained from along the (1k0) row of reflections is shown in Fig. 5B. The reflections between the (1 −1 0), (1 0 0), and (1 1 0) reflections are due to the $0.348b^*$ superlattice, which corresponds to a $2.87 \times b_{sub}$ (*i.e.* ~13 Å) lattice dimension. These supercell reflections also occur along the a^* direction at the same exact position, giving an incommensurate supercell of "$2.87a_{sub} \times 2.87b_{sub}$" However, long exposure axial photographs taken on the X-ray diffractometer for $Na_{0.8}Ag_{1.2}CeTe_4$ suggest that the incommensurate supercell exists only along the *b*-axis, giving a "$1a_{sub} \times 2.87b_{sub}$" supercell. It is likely that the "$2.87a_{sub} \times 2.87b_{sub}$" supercell revealed by electron diffraction comes from twinning involving two crystals each with a "$1a_{sub} \times 2.87b_{sub}$" supercell but rotated 90° with respect to one another according to Scheme 2. At this stage, a decision cannot be made with c2ertainty as to the real identity of the supercell. Undoubtedly we can say that there exists a distortion within the Te net of the $[CeTe_3]$ layer, resulting in oligomerization of the Te atoms such that the larger unit cell better describes the Te net's periodicity. However, given the −0.5 average oxidation state of Te atoms, we may expect the formation of $Te_4{}^{2-}$ units. Since the supercell is both weak and incommensurate, the single crystal X-ray data needed to actually solve the superstructure could not be obtained thus far.

Table 2 Fractional atomic coordinates for $KCuCeTe_4$, $RbCuCeTe_4$, and $Na_{0.8}Ag_{1.2}CeTe_4$ with estimated standard deviations in parentheses

$KCuCeTe_4$

Atom	x	y	z	Occupancy
Ce	0.25	0.25	0.4022(1)	1.0
Te(1)	0.25	0.25	0.5565(1)	1.0
Te(2)	0.25	0.75	0.2827(1)	1.0
Te(3)	0.75	0.25	0.2829(1)	1.0
Te(4)	0.25	0.25	0.0703(1)	1.0
Cu	0.25	0.75	0.9992(3)	1.0
K	0.75	0.75	0.1427(4)	1.0

$RbCuCeTe_4$

Atom	x	y	z	Occupancy
Ce	0.25	0.25	0.4050(1)	1.0
Te(1)	0.25	0.25	0.5548(1)	1.0
Te(2)	0.25	0.75	0.2893(2)	1.0
Te(3)	0.75	0.25	0.2893(2)	1.0
Te(4)	0.25	0.25	0.0677(2)	1.0
Cu	0.25	0.75	0.0001(3)	1.0
Rb	0.75	0.75	0.1475(2)	1.0

$Na_{0.8}Ag_{1.2}CeTe_4$

Atom	x	y	z	Occupancy
Ce	0.25	0.25	0.3966(1)	1.0
Te(1)	0.25	0.25	0.5594(1)	1.0
Te(2)	0.25	0.75	0.2716(1)	1.0
Te(3)	0.75	0.25	0.2711(1)	1.0
Te(4)	0.25	0.25	0.0919(1)	1.0
Ag(1)	0.25	0.75	0.9995(1)	1.0
Ag(2)	0.75	0.75	0.1411(4)	0.2
Na	0.75	0.75	0.1411(4)	0.8

Table 3 Anisotropic displacement parameters (Å) for $KCuCeTe_4$, $RbCuCeTe_4$, and $Na_{0.8}Ag_{1.2}CeTe_4$ with standard deviations in parentheses

$KCuCeTe_4$						
Atom	U11	U22	U33	U12	U13	U23
Ce	0.0129(8)	0.0064(7)	0.022(1)	0	0	0
Te(1)	0.0116(9)	0.0051(8)	0.025(2)	0	0	0
Te(2)	0.028(1)	0.0104(8)	0.025(2)	0	0	0
Te(3)	0.025(1)	0.0114(8)	0.018(2)	0	0	0
Te(4)	0.019(1)	0.0111(9)	0.036(2)	0	0	0
Cu	0.037(2)	0.031(2)	0.032(4)	0	0	0
K	0.032(4)	0.032(4)	0.000(4)	0	0	0
$RbCuCeTe_4$						
aAtom	U11	U22	U33	U12	U13	U23
Ce	0.003(1)	0.009(1)	0.018(2)	0	0	0
Te(1)	0.001(1)	0.007(1)	0.019(2)	0	0	0
Te(2)	0.018(2)	0.017(2)	0.018(2)	0	0	0
Te(3)	0.014(2)	0.017(2)	0.016(2)	0	0	0
Te(4)	0.006(2)	0.019(2)	0.030(2)	0	0	0
Cu	0.015(4)	0.029(4)	0.033(4)	0	0	0
Rb	0.014(2)	0.021(2)	0.025(3)	0	0	0
$Na_{0.8}Ag_{1.2}CeTe_4$						
Atom	U11	U22	U33	U12	U13	U23
Ce	0.0050(6)	0.0064(7)	0.022(1)	0	0	0
Te(1)	0.0050(7)	0.0051(8)	0.025(1)	0	0	0
Te(2)	0.0149(8)	0.0104(8)	0.025(1)	0	0	0
Te(3)	0.0131(8)	0.0114(8)	0.018(1)	0	0	0
Te(4)	0.0125(9)	0.0111(9)	0.036(1)	0	0	0
Ag(1)	0.016(1)	0.031(2)	0.032(1)	0	0	0

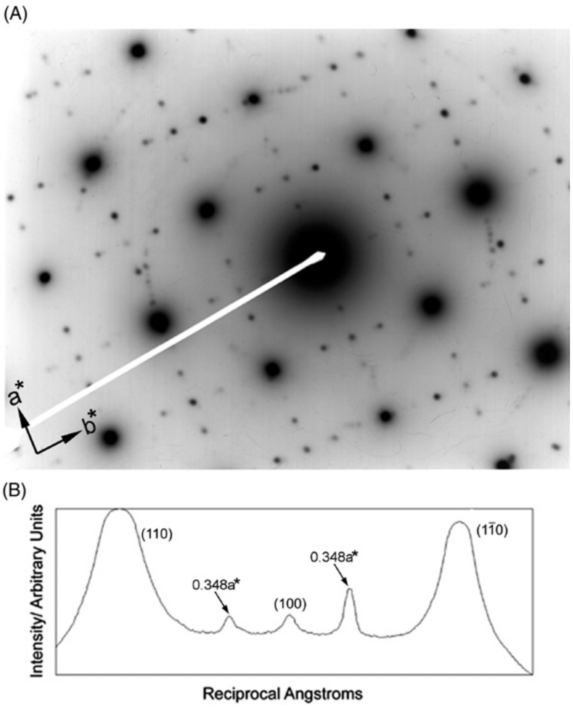

Fig. 5 (A) Selected area electron diffraction pattern of $KCuCeTe_4$ with the beam perpendicular to the layers ([001] direction) showing the $2.87a_{sub} \times 2.87b_{sub}$ superlattice. (B) Densitometric intensity scan along the b^* axis of the electron diffraction pattern showing the (1k0) family of reflections. The three reflections from the sublattice of $KCuCeTe_4$ are indexed. The two weak peaks are from the superlattice with $b_{super} = 2.87b_{sub}$.

Electrical conductivity data as a function of temperature for a hot-pressed (at ~200 °C) pellet of $KCuCeTe_4$ shows a metallic behavior albeit with a relatively low room temperature value of ~180 S cm^{-1}. Therefore, the distortion in the Te layer, which gives rise to the incommensurate superstructure, does not fully open up a gap at the Fermi level of this material, perhaps because the distortion itself is very subtle. Additional work is needed here to understand the detailed crystal structure and observed charge transport properties.

The room temperature electrical conductivity data of $Na_{0.8}Ag_{1.2}CeTe_4$ (pressed pellet) is also moderate at ~100 S cm^{-1} but it exhibits a thermally activated temperature dependence, consistent with the presence of an energy gap. The energy gap in this material is spectroscopically observable at 0.2 eV. The different temperature dependence observed in $KCuCeTe_4$ and $Na_{0.8}Ag_{1.2}CeTe_4$ might be a consequence of the fact that the two compounds possess different modulations in their Te nets. The thermopower data for $Na_{0.8}Ag_{1.2}CeTe_4$ shows a Seebeck coefficient at room temperature of $\sim +21$ μV K^{-1} indicating a p-type conductor.

$K_{2.5}Ag_{4.5}Ln_2Te_9$ (Ln = Ce, La). Another example of an "intergrowth" compound with a square Te net is found in the isostructural $K_{2.5}Ag_{4.5}Ce_2Te_9$ and $K_{2.5}Ag_{4.5}La_2Te_9$ phases, which adopt the orthorhombic space group *Immm*. The layered structure features two "distinct" layers that alternate in an A–B–A–B fashion, see Fig. 6. The slabs are separated by layers of K^+ ions. The first slab, $[CeTe_3]^{0.5-}$, now has an overall negative formal charge in contrast to the neutral version found in $KCuCeTe_4$. This layer contains a Te net that is perfectly square with all Te–Te distances being equal at 3.1806(5) Å. The second slab, $[K_{1.5}Ag_{4.5}Te_3]$, is reminiscent of the one found in KCu_4S_3.[19] The difference, however, is that in $K_{2.5}Ag_{4.5}Ce_2Te_9$, an extra cation exists in-between these "double layers". This cation is disordered between potassium and silver (50 : 50). This layer can also be viewed as being made up of individual cages where now the extra cation centers the cavities of each cage. A more descriptive way of writing this

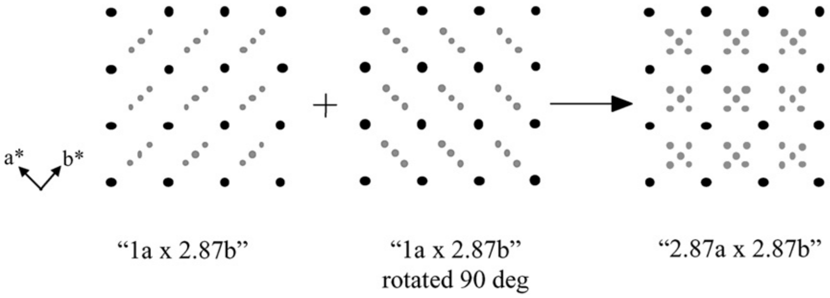

Scheme 2

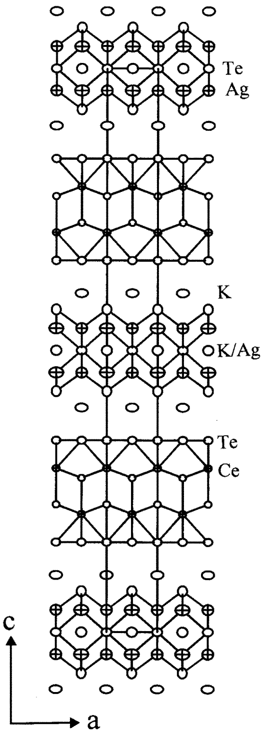

Fig. 6 ORTEP representation of the extended structure of $K_{2.5}Ag_{4.5}Ce_2Te_9$ as seen down the *b*-axis (90% probability ellipsoids). The ellipsoids with solid black shading represent Ce, the crossed ellipsoids represent Ag, the large open ellipsoids represent K (K,Ag) and Te.

formula is therefore $[(K^+)(K_{1.5}Ag_{4.5}Te_3)(CeTe_3{}^{0.5-})_2]$. The crystallographic data, refinement details, fractional atomic coordinates, and anisotropic temperature factors for both compounds are given in Tables 4–6. The $[CeTe_3]^{0.5-}$ layer in $K_{2.5}Ag_{4.5}Ce_2Te_9$ contains a square Te net with the formal oxidation state of the Te atoms in this net being −0.75, different from that in $KCuCeTe_4$. Therefore, here again the Te net is electron deficient and susceptible to distort. To probe for such distortions, electron diffraction studies were performed.

Table 4 Crystallographic data for $K_{2.5}Ag_{4.5}Ce_2Te_9$ and $K_{2.5}Ag_{4.5}La_2Te_9$

	$K_{2.5}Ag_{4.5}Ce_2Te_9$	$K_{2.5}Ag_{4.5}La_2Te_9$
Crystal habit, color	Plate, copper	Plate, copper
Diffractometer	Siemens SMART Platform CCD	Siemens SMART Platform CCD
Radiation	Mo-Kα (0.71069 Å)	Mo-Kα (0.71073 Å)
Crystal size/mm^3	0.31 × 0.22 × 0.04	0.44 × 0.13 × 0.02
Temperature/K	293	293
Crystal system	Orthorhombic	Orthorhombic
Space group	*Immm* (#71)	*Immm* (#71)
a/Å	4.4844(9)	4.5224(6)
b/Å	4.5116(9)	4.5110(9)
c/Å	50.859(10)	50.618(10)
V/Å^3	1029.0(4)	1032.6(4)
Z	2	2
μ/mm^{-1}	21.514	21.166
Index ranges	$-5 \leqslant h \leqslant 5$ $-5 \leqslant k \leqslant 4$ $-65 \leqslant l \leqslant 64$	$-5 \leqslant h \leqslant 5$ $-6 \leqslant k \leqslant 6$ $-65 \leqslant l \leqslant 63$
$2\theta_{max}$/°	50	50
Seconds per frame	60	80
Total data	3348	3271
Unique data	754	777
R(int)	0.0761	0.1186
No. parameters	41	41
Final $R1/wR2^a$/%	8.21/22.40	7.05/17.03
GOF	1.129	1.008

^{a} $R1 = \sum(|F_o| - |F_c|)/\sum|F_o|$ $wR2 = \{\sum[w(F_o{}^2 - F_c{}^2)^2]/\sum[w(F_o{}^2)^2]\}^{1/2}$.

Table 5 Fractional atomic coordinates for $K_{2.5}Ag_{4.5}Ce_2Te_9$ and $K_{2.5}Ag_{4.5}La_2Te_9$ with estimated standard deviations in parentheses

$K_{2.5}Ag_{4.5}Ce_2Te_9$

Atom	*x*	*y*	*z*	Occupancy
Ce	0.0	0	0.2907(1)	1.0
Te(1)	0.0	0	0.2264(1)	1.0
Te(2)	0.5	0.0	0.3403(1)	1.0
Te(3)	0	0.5	0.3404(1)	1.0
Te(4)	0.0	0	0.4274(1)	1.0
Te(5)	0.5	0.5	0.5	1.0
Ag(1)	0.5	0.0	0.4608(1)	1.0
Ag(2)	0	0.5	0.4607(1)	1.0
K(1)	0.5	0.5	0.3985(2)	1.0
K(2)	0.0	0	0.5	0.55(4)
Ag(3)	0.0	0	0.5	0.45(4)

$K_{2.5}Ag_{4.5}La_2Te_9$

Atom	*x*	*y*	*z*	Occupancy
La	0.0	0	0.2912(1)	1.0
Te(1)	0.0	0	0.2261(1)	1.0
Te(2)	0.5	0.0	0.3417(1)	1.0
Te(3)	0	0.5	0.3416(1)	1.0
Te(4)	0.0	0	0.4273(1)	1.0
Te(5)	0.5	0.5	0.5	1.0
Ag(1)	0.5	0.0	0.4607(1)	1.0
Ag(2)	0	0.5	0.4608(1)	1.0
K(1)	0.5	0.5	0.3992(2)	1.0
K(2)	0.0	0	0.5	0.54(3)
Ag(3)	0.0	0	0.5	0.46(3)

Table 6 Anisotropic displacement parameters (Å) for $K_{2.5}Ag_{4.5}Ce_2Te_9$ and $K_{2.5}Ag_{4.5}La_2Te_9$ with standard deviations in parentheses

Atom	U11	U22	U33	U12	U13	U23
Ce	0.021(1)	0.017(1)	0.013(1)	0	0	0
Te(1)	0.019(1)	0.015(1)	0.013(1)	0	0	0
Te(2)	0.038(2)	0.023(1)	0.018(1)	0	0	0
Te(3)	0.043(2)	0.023(1)	0.017(1)	0	0	0
Te(4)	0.030(1)	0.026(1)	0.034(1)	0	0	0
Te(5)	0.036(2)	0.031(2)	0.021(2)	0	0	0
Ag(1)	0.041(2)	0.063(3)	0.034(2)	0	0	0
Ag(2)	0.065(3)	0.038(2)	0.034(2)	0	0	0
K(1)	0.043(5)	0.048(6)	0.021(4)	0	0	0
K(2)	0.040(4)	0.034(4)	0.029(4)	0	0	0
Ag(3)	0.040(4)	0.034(4)	0.029(4)	0	0	0

$K_{2.5}Ag_{4.5}La_2Te_9$

Atom	U11	U22	U33	U12	U13	U23
La	0.005(1)	0.016(1)	0.007(1)	0	0	0
Te(1)	0.004(1)	0.014(1)	0.010(1)	0	0	0
Te(2)	0.018(1)	0.038(1)	0.008(1)	0	0	0
Te(3)	0.019(1)	0.032(1)	0.008(1)	0	0	0
Te(4)	0.011(1)	0.021(1)	0.035(2)	0	0	0
Te(5)	0.028(2)	0.034(2)	0.011(2)	0	0	0
Ag(1)	0.026(2)	0.044(2)	0.033(2)	0	0	0
Ag(2)	0.036(2)	0.036(2)	0.033(2)	0	0	0
K(1)	0.022(4)	0.025(4)	0.027(6)	0	0	0
K(2)	0.017(3)	0.027(3)	0.022(4)	0	0	0
Ag(3)	0.017(3)	0.027(3)	0.022(4)	0	0	0

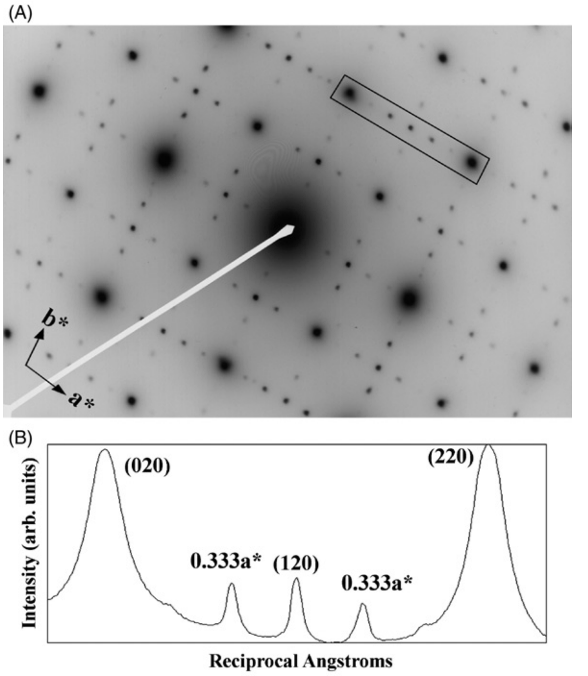

Fig. 7 (A) Selected area electron diffraction pattern of $K_{2.5}Ag_{4.5}Ce_2Te_9$ with the electron beam perpendicular to the layers ([001] direction) showing a twinned $3a_{sub} \times 3b_{sub}$ domain (*i.e.*; two $1a_{sub} \times 3b_{sub}$ supercells that are rotated 90° with respect to one another and superimposed). (B) Densitometric intensity scan along the a^*-axis of the electron diffraction pattern of $K_{2.5}Ag_{4.5}Ce_2Te_9$ (Fig. 7A) (boxed area in photograph) showing the (h 2 0) family of reflections. The three reflections from the sublattice of $K_{2.5}Ag_{4.5}Ce_2Te_9$ are indexed. The two weak peaks are from the $3a_{sub} \times 3b_{sub}$ superlattice.

Fig. 7A shows a typical electron diffraction pattern for $K_{2.5}Ag_{4.5}Ce_2Te_9$ along the *ab*-plane, which indeed contains evidence for a superstructure. A densitometric intensity scan obtained from the (hk0) reciprocal plane along the (h20) row of reflections is shown in Fig. 7B. The reflections between the (020), (120), and (220) reflections are due to a $0.333a^*$ superlattice, which corresponds to a $3 \times a_{sub}$ (*i.e.* ~13.5 Å) lattice dimension. These supercell reflections also occur along the b^* direction, at the same exact position giving a commensurate "$3a_{sub} \times 3b_{sub}$" supercell. However, as was recognized for $KCuCeTe_4$, it is possible that this apparent supercell is an artifact caused by twinning of two domains rotated 90° with respect to one another. Long exposure (>10 000 s) axial photographs were taken on the X-ray diffractometer for many crystals of this compound and the results support this premise, showing supercell reflections along only one axis suggesting the true supercell is that of a "$1a_{sub} \times 3b_{sub}$".

Superstructure of $K_{2.5}Ag_{4.5}Ce_2Te_9$. Because the "$1a_{sub} \times 3b_{sub}$" supercell of $K_{2.5}Ag_{4.5}Ce_2Te_9$ was commensurate, we made attempts to collect good crystallographic data to solve the superstructure and elucidate the Te net distortion.[20] Three possible equivalent monoclinic-C supercells were found, depending on which axis was chosen as the unique axis. They are shown below:

Supercell choice #1	Supercell choice #2	Supercell choice #3
$a = 53.31(1)$ Å	$a = 51.05(1)$ Å	$a = 14.129(3)$ Å
$b = 4.5318(9)$ Å	$b = 13.507(3)$ Å	$b = 50.44(1)$ Å
$c = 13.699(3)$ Å	$c = 4.4800(9)$ Å	$c = 4.4492(9)$ Å
$\alpha = 90°$	$\alpha = 90°$	$\alpha = 90°$
$\beta = 104.84(3)°$	$\beta = 94.91(3)$	$\beta = 108.37(3)°$
$\gamma = 90°$	$\gamma = 90°$	$\gamma = 90°$

Table 7

Subcell		Supercell
$a = 4.4844(9)$ Å		$a' = 14.130(3)$ Å
$b = 4.5116(9)$ Å		$b' = 50.441(10)$ Å
$c = 50.859(10)$ Å		$c' = 4.4492(9)$ Å
$\alpha = 90°$		$\alpha = 90°$
$\beta = 90°$		$\beta = 108.37(3)°$
$\gamma = 90°$		$\gamma = 90°$
Vectorial relationship:		
$a' = -a + 3b$	$b' = c$	$c' = a$

After attempting to solve the superstructure in all three monoclinic cell choices, it was concluded that only supercell choice #3 leads to plausible solution for the superstructure. Supercell choice #1 led to a crystallographic model which made no chemical sense. Many of the assigned atoms were extremely close to one another and the thermal ellipsoids were either too small or too large. Supercell choice #2 gave a plausible solution, however, the Te net had no distortion and the potassium and silver cations were statistically disordered in the same exact fashion as in the subcell. In fact, there was no obvious reason why the unit cell needed to be as large as it was. Finally, when supercell choice #3 was applied, the structural model that was found not only made chemical sense, but exposed the distortions in the Te net. Table 7 gives a comparison of the subcell parameters to those of the correct supercell and the vectorial relationship between the two. The same results were found for $K_{2.5}Ag_{4.5}La_2Te_9$. Complete data collection parameters and details of both structure solutions and refinements are given in Table 8.[21] The fractional atomic coor-

Table 8 Crystallographic data for the "$1a \times 3b$" superstructures of $K_{2.5}Ag_{4.5}Ce_2Te_9$ and $K_{2.5}Ag_{4.5}La_2Te_9$

	$K_{2.5}Ag_{4.5}Ce_2Te_9$ supercell	$K_{2.5}Ag_{4.5}La_2Te_9$ supercell
Crystal habit, color	Plate, copper	Plate, copper
Diffractometer	Siemens SMART Platform CCD	Siemens SMART Platform CCD
Radiation	Mo-Kα (0.71073Å)	Mo-Kα (0.71073Å)
Crystal size/mm^3	$0.31 \times 0.22 \times 0.04$	$0.44 \times 0.13 \times 0.02$
Temperature/K	293	293
Crystal system	Monoclinic	Monoclinic
Space group	$C2/m$ (#12)	$C2/m$ (#12)
a/Å	14.130(3)	14.431(3)
b/Å	50.441(10)	50.728(10)
c/Å	4.4492(9)	4.5186(9)
β/°	108.37(3)	108.42(3)
V/Å^3	3009.4(10)	3118.7(11)
Z	6	6
μ/mm^{-1}	22.192	21.129
Index ranges	$-18 \leqslant h \leqslant 18$ $-65 \leqslant k \leqslant 65$ $-5 \leqslant l \leqslant 5$	$-13 \leqslant h \leqslant 18$ $-65 \leqslant k \leqslant 64$ $-6 \leqslant l \leqslant 5$
$2\theta_{max}$/°	50	50
Seconds per frame	60	80
Total data	11 986	9925
Unique data	3544	3711
R(int)	0.0842	0.1585
No. parameters	136	136
Final $R1/wR2^a$/%	10.41/32.34	9.84/29.29
GOF	1.076	1.039

^{a} $R1 = \sum(|F_o| - |F_c|)/\sum|F_o|$ $wR2 = \{\sum[w(F_o^2 - F_c^2)^2]/\sum[w(F_o^2)^2]\}^{1/2}$.

dinates and anisotropic temperature factors for both compounds are given in Tables 9–12.

The superstructure as seen down the *c*-axis is shown in Fig. 8. Within the $[K_{1.5}Ag_{4.5}Te_3]$ layer, the disorder between the potassium and silver is now partially resolved, see Fig. 9A. While one of the crystallographic sites is now fully assigned as silver, the other site retains a 50/50 disorder between K and Ag. The arrangement of the cations across the layer is now periodic in that every third cation is Ag. From this, it is understandable why the supercell is that of a "$1a_{sub} \times 3b_{sub}$". ". Within the $[CeTe_3]^{0.5-}$ layer, the Te net is now distorted (as expected). A fragment of this layer is shown in Fig. 9B and a comparison between the Te net in the substructure and superstructure is shown in Fig. 10. The net is still fully occupied, but now the Te atoms have oligomerized into infinite zig-zag chains. The Te–Te distances range from 2.922(3)–3.0509(17) Å within the chain and 3.2627–3.3687 Å between the chains.

Table 9 Fractional atomic coordinates for the "$1a_{sub} \times 3b_{sub}$" superstructure of $K_{2.5}Ag_{4.5}Ce_2Te_9$ with estimated standard deviations in parentheses

Atom	*x*	*y*	*z*	Occupancy
Ce(1)	0.5	0.2094(1)	0.5	1.0
Ce(2)	0.3333(1)	0.2906(1)	0.8217(3)	1.0
Te(1)	0.5	0.2734(1)	0.5	1.0
Te(2)	0.3334(1)	0.2264(1)	0.8340(3)	1.0
Te(3)	0.5	0.1597(1)	0.0	1.0
Te(4)	0.3329(1)	0.3404(1)	0.2981(4)	1.0
Te(5)	0.5	0.3406(1)	0	1.0
Te(6)	0.3329(1)	0.1595(1)	0.2941(4)	1.0
Te(7)	0.0	0.5724(1)	−0.5	1.0
Te(8)	0.3332(1)	0.4275(1)	0.8372(3)	1.0
Te(9)	0.5	0.5	0.5	1.0
Te(10)	0.1667(2)	0.5	0.1723(5)	1.0
Ag(1)	0.0	0.5392(1)	0.0	1.0
Ag(2)	0.3330(2)	0.4608(1)	0.3382(5)	1.0
Ag(3)	0.5	0.4606(1)	0.0	1.0
Ag(4)	−0.1664(2)	0.5393(1)	−0.6742(5)	1.0
Ag(5)	0.0	0.5	−0.5	1.0
K(1)	0.5	0.3986(2)	0.5	1.0
K(2)	−0.1666(5)	0.6014(1)	−0.1800(13)	1.0
K(3)	0.3324(4)	0.5	0.8389(9)	0.50(2)
Ag(6)	0.3324(4)	0.5	0.8389(9)	0.50(2)

Table 10 Fractional atomic coordinates for the "$1a_{sub} \times 3b_{sub}$" superstructure of $K_{2.5}Ag_{4.5}La_2Te_9$ with estimated standard deviations in parentheses

Atom	*x*	*y*	*z*	Occupancy
La(1)	0.5	0.2093(1)	0.5	1.0
La(2)	0.3331(1)	0.2914(1)	0.8232(3)	1.0
Te(1)	0.5	0.2742(1)	0.5	1.0
Te(2)	0.3332(1)	0.2262(1)	0.8340(3)	1.0
Te(3)	0.5	0.1586(1)	0.0	1.0
Te(4)	0.3324(1)	0.3417(1)	0.2997(5)	1.0
Te(5)	0.5	0.3423(1)	0.0	1.0
Te(6)	0.3335(1)	0.1585(1)	0.2986(5)	1.0
Te(7)	0.0	0.5736(1)	−0.5	1.0
Te(8)	0.3328(1)	0.4273(1)	0.8377(4)	1.0
Te(9)	0.5	0.5	0.5	1.0
Te(10)	0.1648(2)	0.5	0.1710(6)	1.0
Ag(1)	0.0	0.5404(1)	0.0	1.0
Ag(2)	0.3302(2)	0.4613(1)	0.3381(6)	1.0
Ag(3)	0.5	0.4611(1)	0.0	1.0
Ag(4)	−0.1642(2)	0.5395(1)	−0.6727(6)	1.0
Ag(5)	0.0	0.5	−0.5	1.0
K(1)	0.5	0.4003(2)	0.5	1.0
K(2)	−0.1680(5)	0.6008(1)	−0.1788(12)	1.0
K(3)	0.3298(3)	0.5	0.8345(12)	0.53(2)
Ag(6)	0.3298(3)	0.5	0.8345(12)	0.47(2)

Table 11 Anisotropic displacement parameters (Å) for the "$1a_{sub} \times 3b_{sub}$" superstructure of $K_{2.5}Ag_{4.5}Ce_2Te_9$ with standard deviations in parentheses

Atom	U11	U22	U33	U12	U13	U23
Ce(1)	0.020(1)	0.016(1)	0.024(2)	0	13(1)	0
Ce(2)	0.026(1)	0.019(1)	0.014(1)	1(1)	13(1)	4(1)
Te(1)	0.022(1)	0.017(1)	0.012(1)	0	10(1)	0
Te(2)	0.022(1)	0.020(1)	0.015(1)	2(1)	10(1)	3(1)
Te(3)	0.047(2)	0.025(1)	0.003(2)	0	7(1)	0
Te(4)	0.021(1)	0.022(1)	0.026(2)	2(1)	10(1)	0
Te(5)	0.062(2)	0.023(1)	0.002(2)	0	5(1)	0
Te(6)	0.018(1)	0.023(1)	0.026(1)	4(1)	10(1)	4(1)
Te(7)	0.028(1)	0.044(2)	0.022(2)	0	0(2)	0
Te(8)	0.031(1)	0.042(1)	0.013(1)	−1(1)	1(2)	5(1)
Te(9)	0.041(2)	0.040(2)	0.007(2)	0	−2(2)	0
Te(10)	0.031(1)	0.023(1)	0.024(2)	0	−4(2)	0
Ag(1)	0.051(2)	0.046(2)	0.039(3)	0	−3(2)	0
Ag(2)	0.067(2)	0.044(2)	0.019(2)	−1(1)	−1(2)	5(1)
Ag(3)	0.052(2)	0.041(2)	0.037(2)	0	−5(2)	0
Ag(4)	0.036(2)	0.044(2)	0.047(2)	0	−6(2)	0
Ag(5)	0.062(4)	0.041(3)	0.061(5)	0	−8(4)	0
K(1)	0.051(5)	0.014(3)	0.028(5)	0	−6(5)	0
K(2)	0.066(5)	0.015(3)	0.041(5)	−6(2)	−10(6)	4(2)
K(3)	0.044(4)	0.055(4)	0.017(3)	0	−14(3)	0
Ag(6)	0.044(4)	0.055(4)	0.017(3)	0	−14(3)	0

Electrical conductivity and thermopower measurements were made on both $K_{2.5}Ag_{4.5}La_2Te_9$ and $K_{2.5}Ag_{4.5}Ce_2Te_9$. The electrical conductivity for both compounds decreases with decreasing temperature. Measurements were made on single crystals of $K_{2.5}Ag_{4.5}Ce_2Te_9$, and the results are shown in Fig. 11A. The room temperature conductivity values are ~29 S cm^{-1}. The thermopower data is shown in Fig. 11B and gives a room temperature Seebeck coefficient of ~130 μV K^{-1}. Therefore, the material is best described as a p-type semiconductor. The data are consistent with the existence of an optical

Table 12 Anisotropic displacement parameters (Å) for the "$1a_{sub} \times 3b_{sub}$" superstructure of $K_{2.5}Ag_{4.5}La_2Te_9$ with standard deviations in parentheses

Atom	U11	U22	U33	U12	U13	U23
La(1)	0.012(1)	0.003(1)	0.028(2)	0	20(1)	0
La(2)	0.015(1)	0.004(1)	0.030(1)	1(1)	21(1)	2(1)
Te(1)	0.012(1)	0.005(1)	0.026(2)	0	16(1)	0
Te(2)	0.012(1)	0.005(1)	0.026(1)	−1(1)	16(1)	2(1)
Te(3)	0.061(2)	0.003(1)	0.033(3)	0	22(2)	0
Te(4)	0.012(1)	0.006(1)	0.027(1)	1(1)	16(1)	0
Te(5)	0.059(2)	0.004(1)	0.041(2)	0	9(2)	0
Te(6)	0.012(1)	0.006(1)	0.026(1)	4(1)	17(1)	1(1)
Te(7)	0.019(1)	0.014(1)	0.034(2)	0	21(2)	0
Te(8)	0.021(1)	0.033(1)	0.040(2)	−3(1)	25(2)	1(1)
Te(9)	0.044(2)	0.009(2)	0.049(4)	0	23(2)	0
Te(10)	0.028(1)	0.007(1)	0.043(2)	0	22(2)	0
Ag(1)	0.041(2)	0.016(2)	0.024(3)	0	8(2)	0
Ag(2)	0.040(2)	0.037(2)	0.031(2)	−3(1)	2(2)	−2(1)
Ag(3)	0.037(2)	0.041(2)	0.041(4)	0	4(3)	0
Ag(4)	0.029(1)	0.026(1)	0.042(2)	−5(1)	11(2)	−9(1)
Ag(5)	0.055(3)	0.031(3)	0.059(6)	0	39(4)	0
K(1)	0.018(4)	0.025(5)	0.013(5)	0	−20(4)	0
K(2)	0.031(3)	0.012(3)	0.010(2)	2(2)	−20(6)	6(2)
K(3)	0.025(3)	0.016(3)	0.049(5)	0	27(3)	0
Ag(6)	0.025(3)	0.016(3)	0.049(5)	0	27(3)	0

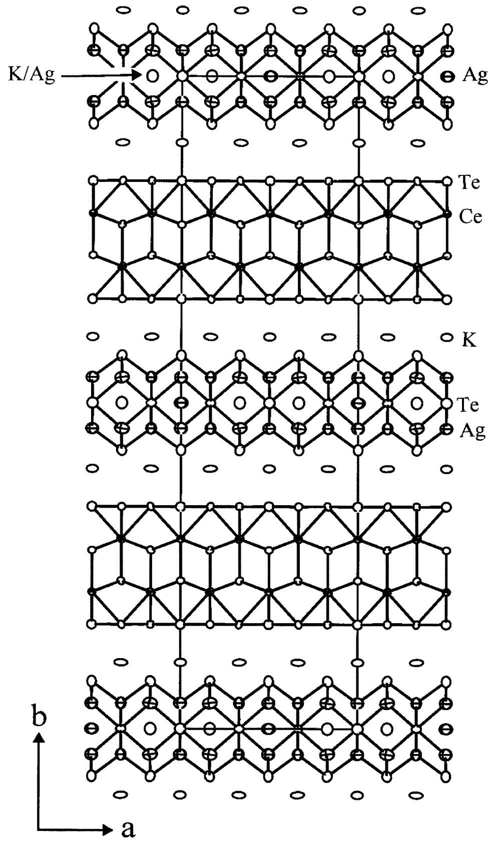

Fig. 8 ORTEP representation of the "$1a_{sub} \times 3b_{sub}$" superstructure of $K_{2.5}Ag_{4.5}Ce_2Te_9$ as seen down the *c*-axis (75% probability ellipsoids). The ellipsoids with black shading represent Ce, the crossed ellipsoids represent Ag, the large open ellipsoids represent K (K,Ag) and Te

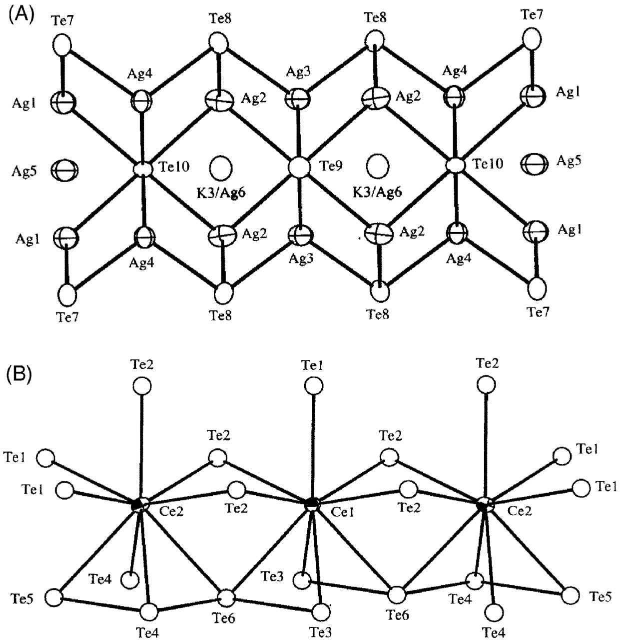

Fig. 9 ORTEP representation (50% probability ellipsoids) of (A) The $[K_{1.5}Ag_{4.5}Te_3]$ layer of the $1a_{sub} \times 3b_{sub}$ superstructure of $K_{2.5}Ag_{4.5}Ce_2Te_9$, and (B) a fragment of the $[CeTe_3^{0.5-}]$ layer of the $1a_{sub} \times 3b_{sub}$ superstructure of $K_{2.5}Ag_{4.5}Ce_2Te_9$ highlighting the particular coordination environment of Ce. The ellipsoids with octant shading represent Ce, the crossed ellipsoids represent Ag, and the large open ellipsoids represent (K,Ag) mixed site and Te.

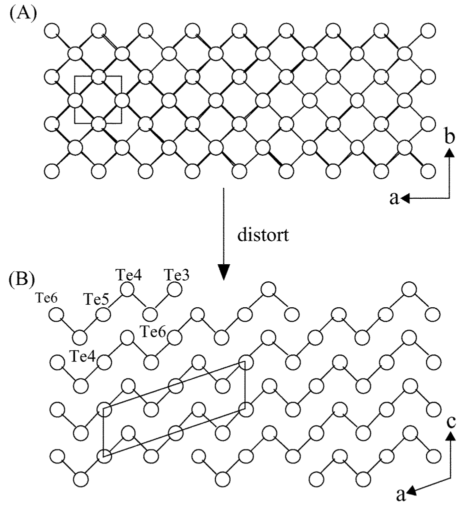

Fig. 10 View of the Te "nets" in (A) the substructure of $K_{2.5}Ag_{4.5}Ce_2Te_9$ and (B) the $1a_{sub} \times 3b_{sub}$ superstructure of $K_{2.5}Ag_{4.5}Ce_2Te_9$.

bandgap of 0.3 eV. Similar results were found for room temperature pressed pellets of the La analog, see Fig. 12A, with room temperature conductivity values of ~14 S cm^{-1}. The thermopower data for a pressed pellet of the La analog is shown in Fig. 12B. While the magnitudes are very similar to that of the cerium analog (~170 μV K^{-1} at 300 K), the slopes are somewhat different. For the lanthanum analog, there is a

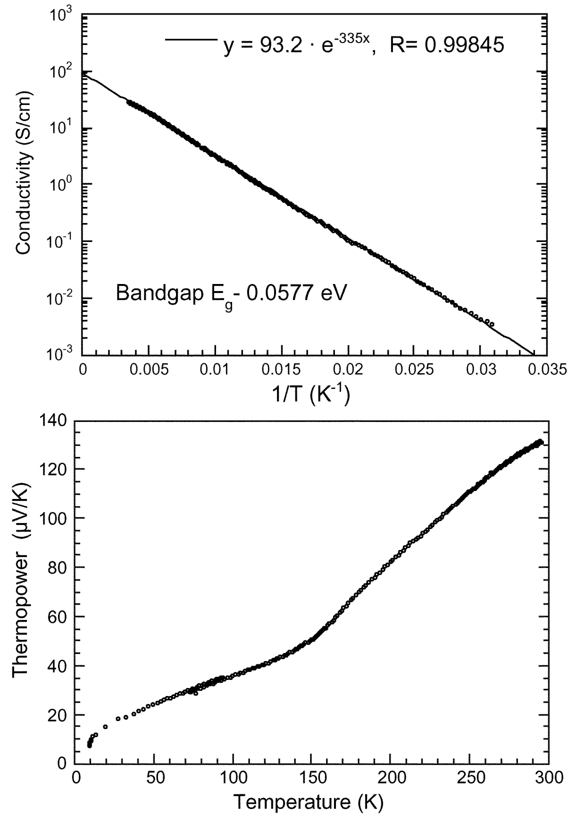

Fig. 11 (A) Four-probe electrical conductivity data for a crystal of $K_{2.5}Ag_{4.5}Ce_2Te_9$ as a function of temperature. The "bandgap" value of ~0.06 eV calculated from the data is not the semiconductor gap but the carrier activation energy gap which is not necessarily the same because of mid-gap impurity levels created by inadvertent doping. (B) Thermopower data of a crystal of $K_{2.5}Ag_{4.5}Ce_2Te_9$ as a function of temperature.

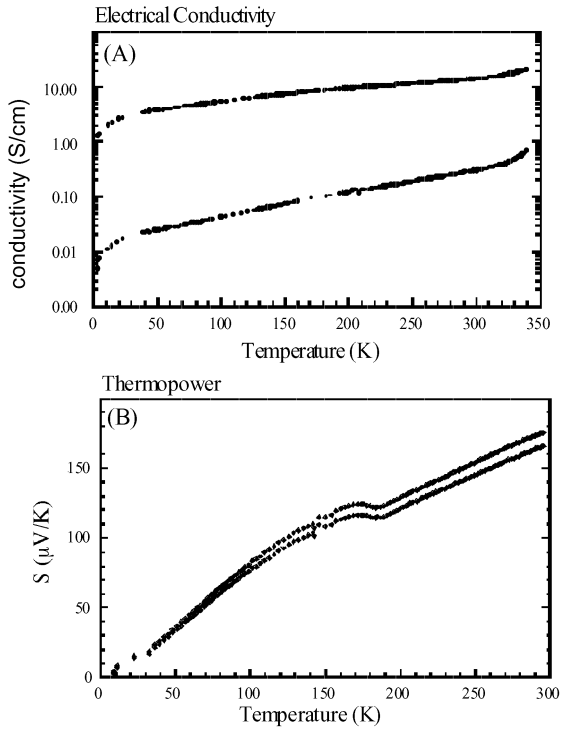

Fig. 12 (A) Four-probe electrical conductivity data of two room temperature pressed pellets of $K_{2.5}Ag_{4.5}La_2Te_9$ as a function of temperature. (B) Thermopower data of a room temperature pressed pellet of $K_{2.5}Ag_{4.5}La_2Te_9$ as a function of temperature. The two different data sets are from two different pressed pellet samples. The variance could be due to either different doping or to variance in the pressure applied during pellet fabrication.

reproducible convex dip in the data around 170 K. The origin of this dip is yet unknown.

Europium compounds

The square net motif of the Te atoms seems to persist across the rare earth series. Although the entire series was not examined, europium was deemed to represent an important stop because of its ability to adopt both +3 and +2 formal oxidation states. In the presence of tellurium, we expected a +2 oxidation state and thus a departure from the motif afforded by the Ln^{3+} cations. This approach yielded several new compounds, all of which contained square Te nets: $Cu_{0.66}EuTe_2$, KCu_2EuTe_4, $Na_{0.2}Ag_{2.8}EuTe_4$ and $K_{0.65}Ag_2Eu_{1.35}Te_4$. The latter is so well ordered that the modulation in the Te net could be directly obtained from the X-ray crystallographic analysis.

$Cu_{0.66}EuTe_2$. The structure of $Cu_{0.66}EuTe_2$ is shown in Fig. 13. It adopts the tetragonal $CaMnBi_2$ structure-type (space group *P*4/*mmn*) and features 8-coordinate europium atoms in a square-antiprismatic coordination environment of tellurium. The europium atoms are sandwiched between a $[CuTe]^-$ anti-PbO type layer and a flat square net of Te atoms. The Te–Te distances in the net are all equal at 3.168(1) Å, a value substantially longer than the normal Te–Te bond of 2.8 Å, yet much shorter than the van der Waals contact of 3.8–4.0 Å. The bonds around the europium atoms have been omitted in Fig. 13 to highlight the stacking of each individual layer. The copper site is only partially occupied and refines to a value of 0.66.[22] Interestingly, this structure type has been encountered in the family of antimonides M_xLaSb_2 (M = Zn, Co, Mn, and Cu; $x = 0.52–0.87$).[23] In all of these phases, the transition metal site is partially occupied. $Cu_{0.66}EuTe_2$ appears to be the first telluride member of this family. Assuming $[Cu_{0.66}Te]^{-1.33}$ and Eu^{2+}, we can calculate a $Te^{-0.66}$ average charge per atom and therefore a distortion is expected.

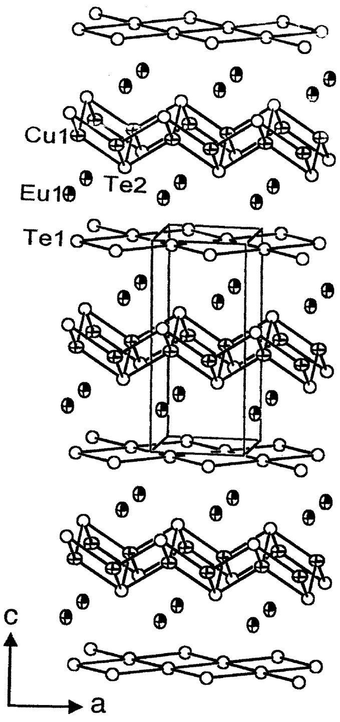

Fig. 13 ORTEP representation of the structure of $Cu_{0.66}EuTe_2$ as seen down the *b*-axis (70% ellipsoids). The ellipsoids with octant shading represent Eu atoms. The crossed ellipsoids represent Cu atoms and the open ellipsoids represent Te atoms.

$A_xM_{(3-x)}EuTe_4$. The structure of KCu_2EuTe_4 is actually polar (space group *P*4*mm*), a unique characteristic in this group of compounds (see Fig. 14). The bonds to europium

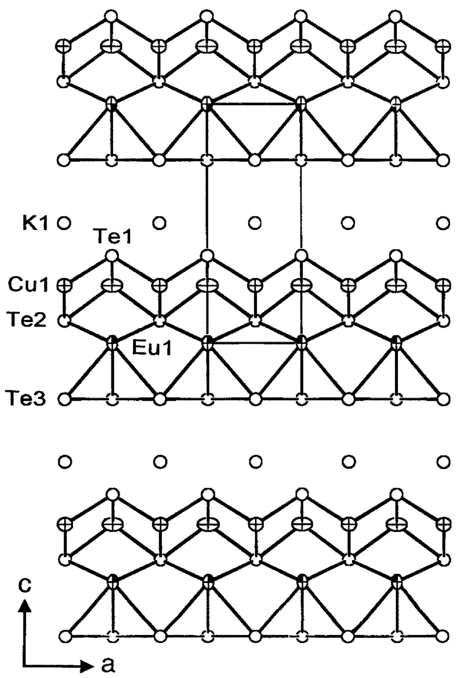

Fig. 14 ORTEP representation of the structure of KCu_2EuTe_4 (70% ellipsoids) as viewed down the *b*-axis. The ellipsoids with octant shading represent Eu atoms, the crossed ellipsoids represent Cu atoms and the open ellipsoids represent Te and K atoms. The Te3 atoms make the square Te net.

have now been included to highlight its square antiprismatic coordination environment. The structure of KCu_2EuTe_4 can be derived from that of $Cu_{0.66}EuTe_2$ by first restoring the Cu site to full occupancy and then replacing every other layer of europium atoms with potassium. This replacement of atoms is reasonable if we compare the effective ionic radii of Eu^{2+} (1.17 Å) to that of K^+ (1.38 Å). Thus, we can expect the europium to be truly divalent since a trivalent europium (ionic radius 0.947 Å) is too small for such a site. As a result, this replacement has caused the *n*-glide plane to be lost in moving from $Cu_{0.66}EuTe_2$ to KCu_2EuTe_4 and the symmetry to change from centrosymmetric to non-centrosymmetric. For structural details see Table 13.

$Na_{0.2}Ag_{2.8}EuTe_4$ is isostructural to KCu_2EuTe_4, but now there exists some mixed occupancy on the Na site with Ag, which can be explained again by the similar effective ionic radii of the two metals.[24] The fractional atomic coordinates, anisotropic temperature factors for all Eu compounds presented thus far are given in Tables 14 and 15.

Because of the tetragonal symmetry, the Te nets in both KCu_2EuTe_4 and $Na_{0.2}Ag_{2.8}EuTe_4$ appear perfectly square with all shortest Te–Te distances at 3.1371(4) Å and 3.1497(4) Å, respectively. Of course we know by now that this is an artifact and we expect some sort of modulation.[8,25] Electron diffraction experiments on very thin crystals of KCu_2EuTe_4 and $Na_{0.2}Ag_{2.8}EuTe_4$ clearly showed evidence for a superstructure. Fig. 15A shows a typical electron diffraction pattern for KCu_2EuTe_4 depicting the (*hk*0) zone. The weak spots that appear in this micrograph occur along both the a^* and b^* direction and correspond to a $0.286a^* \times 0.286b^*$ superlattice. This value corresponds to 3.496 in real space and therefore the supercell can be modeled as $\sim 3.496a_{sub} \times 3.496b_{sub}$. However, many of the crystals examined under the electron beam were highly microtwinned causing the modulation to appear along both the a^* and b^* axes. This pattern probably arises from the superimposition of two $1a_{sub} \times 3.496\ b_{sub}$ patterns that are rotated 90° with respect to one another, as has been found for $K_{0.33}Ba_{0.67}AgTe_2$.[3a,18] The electron diffraction pattern of $Na_{0.2}Ag_{2.8}EuTe_4$, shown in Fig. 15B, was taken from a very thin region of a single crystal and contains superlattice spots along only one direction. Due to the tetragonal symmetry of the subcell, the propensity of these crystals to twin is seemingly high and a micrograph of this sort showing single crystal domains is difficult to obtain. The spots in this diffraction pattern correspond again to a $1a_{sub} \times 3.496b_{sub}$ superlattice and it can therefore be concluded that both of these compounds exhibit the same superlattice. Fig. 15C is a densitometric intensity scan along the b^*-axis of the electron diffraction pattern of $Na_{0.2}Ag_{2.8}EuTe_4$. The three reflections from the tetragonal sublattice are indexed. The four weak peaks are from the supercell along this axis.

The issue of charge balancing in all three cases is anything but trivial. The non-stoichiometry in $Cu_{0.66}EuTe_2$ must be taken into consideration, in addition to the superstructures of KCu_2EuTe_4 and $Na_{0.2}Ag_{2.8}EuTe_4$, when assigning formal charges. Since the actual superstructures have not yet been determined, only the average charge per tellurium atom in the net can be calculated, assuming Cu^+, Ag^+, and Eu^{2+}.[26] For $Cu_{0.66}EuTe_2$, it is best to keep the structure in mind when balancing the charges. The formal charges on KCu_2EuTe_4 and $Na_{0.2}Ag_{2.8}EuTe_4$ can be assigned similarly; $[(K^+)(CuTe^-)_2(Eu^{2+})(Te^{-0.5})_2]$ and $[(Na^+{}_{0.2}Ag^+{}_{0.8})(AgTe^-)_2(Eu^{2+})(Te^{-0.5})]$. Based on these formulations, the average charge per Te atom in the square net changes from −0.66 in $Cu_{0.66}EuTe_2$ to −0.5 in KCu_2EuTe_4 and $Na_{0.2}Ag_{2.8}EuTe_4$. A net of Te atoms with a −0.67 average charge may be expected to give a modulation that produces $Te_3{}^{2-}$ species, whereas a −0.50 average charge should give a different distortion pattern, perhaps $Te_4{}^{2-}$ species. However, a full crystallographic analysis would be required to reveal the reasons for the observed superstructures.

The infrared spectrum of $Na_{0.2}Ag_{2.8}EuTe_4$ reveals an abrupt optical transition at 0.24 eV that could be assigned to a semiconductor bandgap and in this sense it is consistent with the charge transport properties observed for this material. Electrical conductivity and thermoelectric power data were measured as a function of temperature for pressed pellets of KCu_2EuTe_4 and $Na_{0.2}Ag_{2.8}EuTe_4$, see Fig. 16. For KCu_2EuTe_4, the data

Table 13 Crystallographic data for $Cu_{0.66}EuTe_2$, KCu_2EuTe_4, and $Na_{0.2}Ag_{2.8}EuTe_4$

	$Cu_{0.66}EuTe_2$	KCu_2EuTe_4	$Na_{0.2}Ag_{2.8}EuTe_4$
Crystal habit, color	Plate, copper	Plate, copper	Plate, copper
Diffractometer	Rigaku AFC6s	Rigaku AFC6S	Siemens SMART Platform CCD
Radiation	Mo-Kα (0.71069Å)	Mo-Kα (0.71073 Å)	Mo-Kα (0.71073 Å)
Crystal size/mm^3	0.44 × 0.13 × 0.02	0.40 × 0.40 × 0.04	0.13 × 0.39 × 0.01
Temperature/K	293	293	293
Crystal system	Tetragonal	Tetragonal	Tetragonal
Space group	*P*4/*mmm* (#129)	*P*4*mm* (#99)	*P*4*mm* (#99)
a/Å	4.4810(16)	4.4365(6)	4.4544(6)
b/Å	4.4810(16)	4.4365(6)	4.4544(6)
c/Å	10.260(3)	11.365(2)	11.106(2)
V/Å^3	206.02(12)	223.69(6)	220.37(6)
Z	2	1	1
μ/mm^{-1}	32.196	24.789	26.044
Index ranges	$0 \leqslant h \leqslant 5$	$-5 \leqslant h \leqslant 5$	$-5 \leqslant h \leqslant 5$
	$-5 \leqslant k \leqslant 5$	$-5 \leqslant k \leqslant 5$	$-5 \leqslant k \leqslant 5$
	$-11 \leqslant l \leqslant 12$	$-13 \leqslant l \leqslant 13$	$-13 \leqslant l \leqslant 14$
$2\theta_{max}$/°	50	50	50
Seconds per frame	N/A	N/A	40
Total data	1169	1597	1941
Unique data	141	295	361
R(int)	0.1083	0.1473	0.1114
No. parameters	12	23	23
Final $R1/wR2^a$/%	7.94/25.07	7.35/17.88	7.30/20.35
GOF	1.477	1.198	1.078

[a] $R1 = \sum(|F_o| - |F_c|)/\sum|F_o|$ $wR2 = \{\sum[w(F_o{}^2 - F_c{}^2)^2]/\sum[w(F_o{}^2)^2]\}^{1/2}$.

Table 14 Fractional atomic coordinates for $Cu_{0.66}EuTe_2$, KCu_2EuTe_4, and $Na_{0.2}Ag_{2.8}EuTe_4$ with estimated standard deviations in parentheses

$Cu_{0.66}EuTe_2$

Atom	x	y	z	Occupancy
Eu	0.25	−0.25	0.7402(5)	1.0
Te(1)	0.75	0.25	0	1.0
Te(2)	0.25	0.25	0.6417(6)	1.0
Cu	−0.25	0.25	0.5	0.66

KCu_2EuTe_4

Atom	x	y	z	Occupancy
Eu	0.0	0.0	0.0000(3)	1.0
Te(1)	0.0	0.0	0.3661(4)	1.0
Te(2)	0.5	0.5	0.0940(1)	1.0
Te(3)	0.5	0.0	0.7655(2)	1.0
Cu	0.5	0.0	0.2416(6)	1.0
K	0.5	0.5	0.5029(18)	1.0

$Na_{0.2}Ag_{2.8}EuTe_4$

Atom	x	y	z	Occupancy
Eu	0.0	0.0	0.0012(6)	1.0
Te(1)	0.0	0.0	0.4339(4)	1.0
Te(2)	0.5	0.5	0.1014(5)	1.0
Te(3)	0.5	0.0	0.7729(7)	1.0
Ag(1)	0.5	0.0	0.2768(8)	1.0
Ag(2)	0.5	0.5	0.5335(5)	0.79
Na	0.5	0.5	0.5335(5)	0.21

Table 15 Anisotropic displacement parameters (Å) for $Cu_{0.66}EuTe_2$, KCu_2EuTe_4, and $Na_{0.2}Ag_{2.8}EuTe_4$with standard deviations in parentheses

$Cu_{0.66}EuTe_2$

Atom	U11	U22	U33	U12	U13	U23
Eu	0.021(2)	0.021(2)	0.033(3)	0	0	0
Te(1)	0.030(2)	0.030(2)	0.018(4)	0	0	0
Te(2)	0.019(2)	0.019(2)	0.027(5)	0	0	0
Cu	0.036(6)	0.036(6)	0.019(9)	0	0	0

KCu_2EuTe_4

Atom	U11	U22	U33	U12	U13	U23
Eu	0.016(1)	0.016(1)	0.034(2)	0	0	0
Te(1)	0.020(1)	0.020(1)	0.035(2)	0	0	0
Te(2)	0.019(1)	0.018(1)	0.032(2)	0	0	0
Te(3)	0.021(1)	0.021(1)	0.031(2)	0	0	0
Cu	0.032(3)	0.065(4)	0.027(3)	0	0	0
K	0.016(3)	0.016(3)	0.036(5)	0	0	0

$Na_{0.2}Ag_{2.8}EuTe_4$

Atom	U11	U22	U33	U12	U13	U23
Eu	0.024(2)	0.024(2)	0.064(5)	0	0	0
Te(1)	0.012(2)	0.012(2)	0.013(3)	0	0	0
Te(2)	0.001(1)	0.001(1)	0.028(3)	0	0	0
Te(3)	0.014(2)	0.016(2)	0.019(2)	0	0	0
Ag(1)	0.020(2)	0.020(2)	0.016(2)	0	0	0
Ag(2)	0.009(2)	0.009(2)	0.000(3)	0	0	0
Na	0.009(2)	0.009(2)	0.000(3)	0	0	0

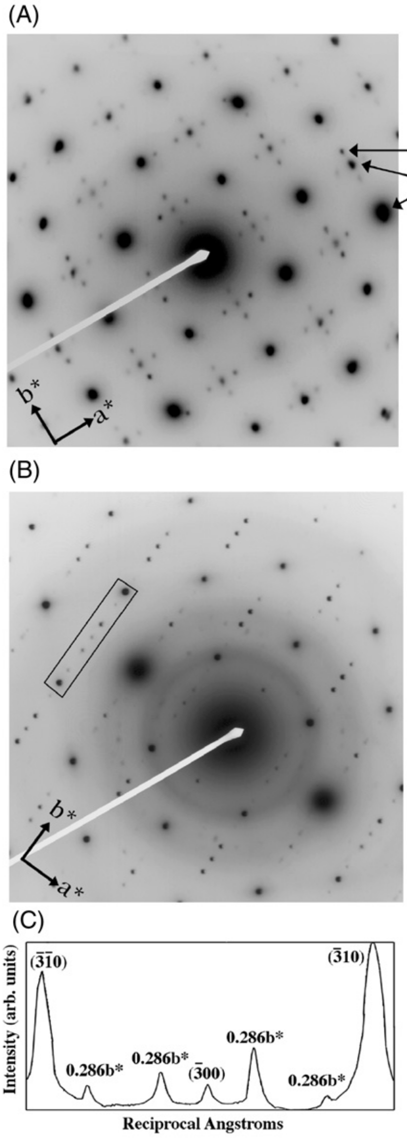

Fig. 15 (A) Selected area electron diffraction pattern of KCu_2EuTe_4 with the electron beam perpendicular to the layers ([001] direction) showing a twinned $3.496a_{sub} \times 3.496b_{sub}$ domain (*i.e.*; two $1a_{sub} \times 3.496b_{sub}$ supercells that are rotated 90° with respect to one another and superimposed). (B) Selected area electron diffraction pattern of $Na_{0.2}Ag_{2.8}EuTe_4$ with the electron beam perpendicular to the layers ([001] direction) showing the $1a \times 3.496b$ superlattice of single crystal region. (C) Densitometric intensity scan along the b^*-axis of the electron diffraction pattern of $Na_{0.2}Ag_{2.8}EuTe_4$ (Fig. 15B) (boxed area in photograph) showing the (−3 k 0) family of reflections. The three reflections from the sublattice of $Na_{0.2}Ag_{2.8}EuTe_4$ are indexed. The four weak peaks are from the $1a \times 3.496b$ superlattice.

suggest p-type metallic or semimetallic behavior with a room temperature conductivity of 165 S cm^{-1} and a Seebeck coefficient of +23 μV K^{-1}. This agrees with the fact that no optical bandgap was detected for this material in the region 0.1 to 1.0 eV. The data for $Na_{0.2}Ag_{2.8}EuTe_4$ suggest p-type semiconducting behavior with a room temperature conductivity value of 12 S cm^{-1} and a Seebeck coefficient of +70 μV K^{-1}. Incidentally, the presence of a band gap was detected for this compound at ~0.24 eV. In the absence of critical crystallographic information as to the exact nature of the modulations in these phases and particularly in KCu_2EuTe_4 it is not possible to explain the lack of optical band gap in this material.

$K_{0.65}Ag_2Eu_{1.35}Te_4$: A well resolved distortion. The structure of $K_{0.65}Ag_2Eu_{1.35}Te_4$ as viewed down the *a*-axis is shown in

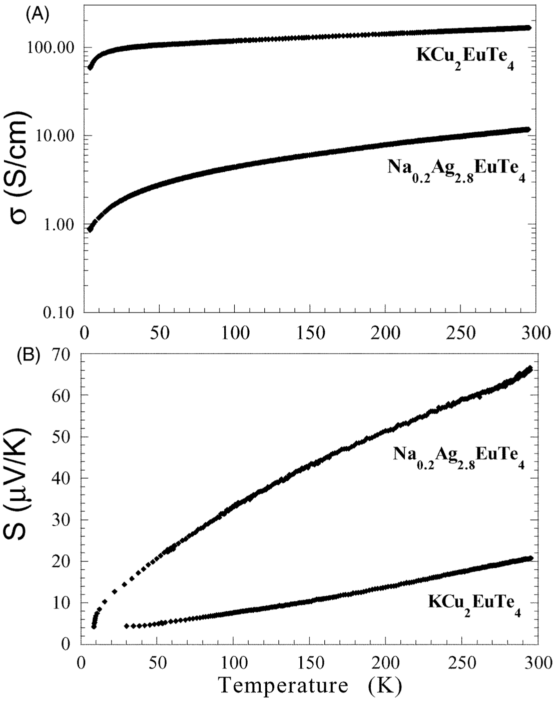

Fig. 16 (A) Four-probe, electrical-conductivity data of room temperature pressed pellets of KCu_2EuTe_4 and $Na_{0.2}Ag_{2.8}EuTe_4$ as a function of temperature. (B) Thermopower data of room temperature pressed pellets of KCu_2EuTe_4 and $Na_{0.2}Ag_{2.8}EuTe_4$ as a function of temperature.

Fig. 17. Refinement details can be found in Table 16. At first glance, the structure may appear very similar to that of KCu_2EuTe_4. The layers are polar and are composed of square antiprismatic europium atoms sandwiched between a $[AgTe]^-$ anti-PbO type layer and a flat Te net, see Fig. 18A. However, unlike KCu_2EuTe_4 which has perfectly square Te net, The Te net in $K_{0.65}Ag_2Eu_{1.35}Te_4$ is already modulated, see Fig. 19. The Te atoms have oligomerized into trimers and heptamers, which alternate across the layer in a 1 : 1 ratio. In addition to alternating with each other, they also alternate back and forth in orientation and this alternating pattern persists along both the *b*- and *c*-axes. Therefore, in order to re-describe the periodicity of the structure, the *b*-axis must be multiplied by 10 and the *c*-axis by 2. Conceptually, the unit cell of $K_{0.65}Ag_2Eu_{1.35}Te_4$ can be considered as a $1a_{sub} \times 10b_{sub} \times 2c_{sub}$ supercell over that of KCu_2EuTe_4. However, a direct comparison cannot be made because KCu_2EuTe_4 possesses its own supercell of $1a_{sub} \times 3.496b_{sub}$. The reason that the two compounds possess different supercells and therefore different modulated Te nets is because the charge per Te atom on the net is different for each (−0.5 for KCu_2EuTe_4 and −0.675 for $K_{0.65}Ag_2Eu_{1.35}Te_4$). This difference is due to the fact that in $K_{0.65}Ag_2Eu_{1.35}Te_4$ the potassium sites are disordered with europium (65% K : 35% Eu). Because potassium is monovalent and europium is divalent, the disordering of these elements affects the overall charge on the Te net. These disordered sites, much like the pure Eu sites, are 8-coordinate square antiprismatic with Te. Complete data collection parameters and details of the solution and refinement for $K_{0.65}Ag_2Eu_{1.35}Te_4$

Table 16 Crystallographic data for $K_{0.65}Ag_2Eu_{1.35}Te_4$

$K_{0.65}Ag_2Eu_{1.35}Te_4$	
Crystal habit, color	Plate, copper
Diffractometer	Siemens SMART Platform CCD
Radiation	Mo-Kα (0.71073 Å)
Crystal size/mm^3	0.21 × 0.21 × 0.02
Temperature/K	293
Crystal system	Orthorhombic
Space group	*Abm*2 (#39)
a/Å	4.4989(9)
b/Å	45.279(9)
c/Å	22.799(5)
V/Å^3	4644.4(16)
Z	20
μ/mm^{-1}	25.682
Index ranges	$-5 \leqslant h \leqslant 5$ $-57 \leqslant h \leqslant 57$ $-29 \leqslant h \leqslant 29$
$2\theta_{max}$/°	50
Seconds per frame	80
Total data	22 152
Unique data	5116
R(int)	0.0824
No. parameters	180
Final $R1/wR2^a$/%	6.46/27.80
Goof	2.148

[a] $R1 = \sum(|F_o| - |F_c|)/\sum|F_o|$ $wR2 = \{\sum[w(F_o^2 - F_c^2)^2]/\sum[w(F_o^2)^2]\}^{1/2}$.

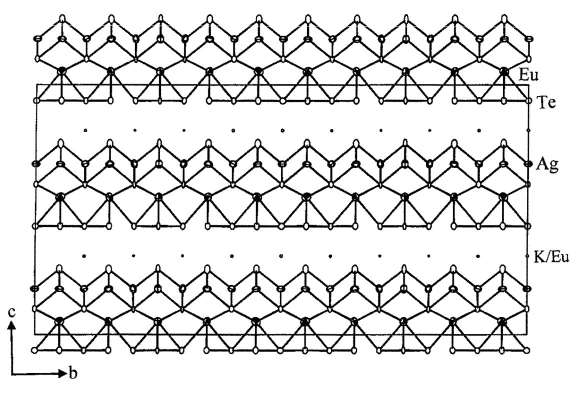

Fig. 17 ORTEP representation of the structure of $K_{0.65}Ag_2Eu_{1.35}Te_4$ (80% ellipsoids) as viewed down the *a*-axis. The ellipsoids with octant shading represent Eu atoms, the crossed ellipsoids represent Ag atoms and the open ellipsoids represent Te and K/Eu atoms.

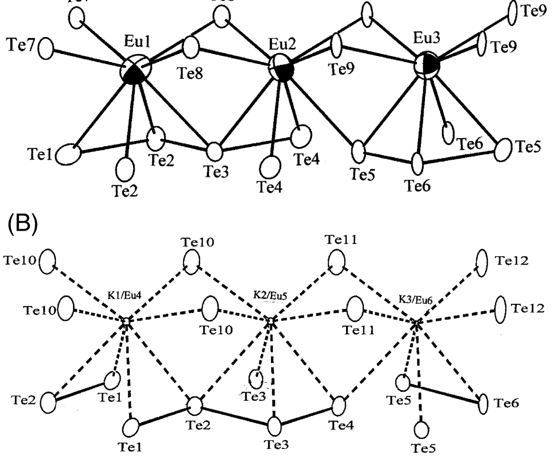

Fig. 18 ORTEP representation of (A) the coordination environment around Eu in $K_{0.65}Ag_2Eu_{1.35}Te_4$ and (B) the coordination environment around K/Eu in $K_{0.65}Ag_2Eu_{1.35}Te_4$ (90% ellipsoids for both). The ellipsoids with octant shading represent Eu atoms and the small and large open ellipsoids represent K/Eu and Te, respectively.

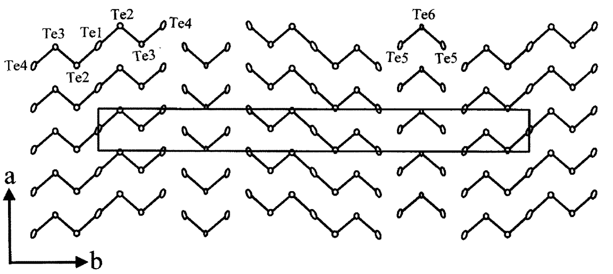

Fig. 19 ORTEP representation of the Te "net" of $K_{0.65}Ag_2Eu_{1.35}Te_4$ as seen along the *ab* plane (80% probability ellipsoids) highlighting the arrangement of trimers and heptamers.

are given in Table 16, while fractional atomic coordinates and anisotropic temperature factors are given in Tables 17 and 18. While we believe that this structure model is a very close approximation to the true structure, it is possible that there exists an additional modulation that is either incommensurate or too weak to be observed by X-rays, which currently we do not account for. Considering that there still exists some disorder on the potassium sites with europium, this suspected supercell could also succeed in resolving this disorder.

Electrical conductivity and thermoelectric power data were measured as a function of temperature for two single crystals of $K_{0.65}Ag_2Eu_{1.35}Te_4$ (see Fig. 20). The conductivity data suggest semiconducting behavior with a sharp decline below 150 K. However, the magnitudes differ significantly from crystal to crystal. The room temperature values varied from 30 S cm^{-1} to 130 S cm^{-1}.

The thermopower data for two crystals are shown in Fig. 20B. Although the conductivity values exhibit a wide range, the thermopower values are consistent with a very narrow range of 170–190 $\mu V\ K^{-1}$ at room temperature. The positive sign and decreasing Seebeck coefficient with falling temperature is consistent with a semiconductor and suggest p-type behavior.

Table 17 Fractional atomic coordinates for $K_{0.65}Ag_2Eu_{1.35}Te_4$ with estimated standard deviations in parentheses

Atom	*x*	*y*	*z*	Occupancy
Eu(1)	0.5070(13)	0.9500(1)	1.0527(2)	1.0
Eu(2)	0.5054(13)	0.8500(1)	1.0526(1)	1.0
Eu(3)	0.4887(14)	0.75	1.0526(1)	1.0
Te(1)	0.50	1.00	0.9358(3)	1.0
Te(2)	0.0297(7)	0.9497(1)	09 365(2)	1.0
Te(3)	0.4629(7)	0.9001(1)	0.9358(1)	1.0
Te(4)	0.0149(9)	0.8501(1)	0.9367(2)	1.0
Te(5)	0.5253(8)	0.7997(1)	0.9360(2)	1.0
Te(6)	0.9614(9)	0.75	0.9367(2)	1.0
Te(7)	1.00	1.00	1.1036(2)	1.0
Te(8)	1.0057(6)	0.9000(1)	1.1036(1)	1.0
Te(9)	−0.0037(6)	0.7000(1)	1.1032(1)	1.0
Te(10)	0.5041(6)	0.9500(1)	1.2635(2)	1.0
Te(11)	0.5010(6)	0.8500(1)	1.2630(2)	1.0
Te(12)	0.4948(9)	0.75	1.2632(2)	1.0
Ag(1)	0.5	1.00	1.1841(3)	1.0
Ag(2)	1.0020(20)	0.9500(1)	1.1839(2)	1.0
Ag(3)	−0.5130(20)	0.8999(1)	1.1845(2)	1.0
Ag(4)	0.9974(14)	0.8500(1)	1.1839(2)	1.0
Ag(5)	0.4910(16)	0.7000(1)	1.1847(2)	1.0
Ag(6)	0.0020(30)	0.75	1.1843(3)	1.0
K(1)	0.0	1.00	0.8168(2)	0.638(16)
Eu(4)	0.0	1.00	0.8168(2)	0.362(16)
K(2)	−0.138(8)	0.9000(1)	0.8162(2)	0.650(10)
Eu(5)	−0.138(8)	0.9000(1)	0.8162(2)	0.350(10)
K(3)	1.0093(8)	0.7998(1)	0.8170(2)	0.656(11)
Eu(6)	1.0093(8)	0.7998(1)	0.8170(2)	0.344(11)

Conclusions

Several new compounds of the type $A_wM_xLn_yTe_z$ have been discovered through the use of alkali metal/polytelluride fluxes. The common theme that runs through these compounds is the existence of a square Te net. These Te nets are always distorted in ways that are highly dependent on the average charge per Te

Table 18 Anisotropic displacement parameters (Å) for $K_{0.65}Ag_2Eu_{1.35}Te_4$ with standard deviations in parentheses

Atom	U11	U22	U33	U23	U13	U12
Eu(1)	0.027(1)	0.0035(1)	0.030(1)	−0.0004(1)	−0.0007(1)	0.0005(1)
Eu(2)	0.033(2)	0.0021(1)	0.030(1)	0.0003(2)	0.0000(2)	0.0002(1)
Eu(3)	0.036(2)	0.0023(1)	0.028(2)	0	−0.0003(2)	0
Te(1)	0.039(3)	0.0017(2)	0.015(3)	0	0	0.0015(2)
Te(2)	0.014(1)	0.0012(1)	0.021(2)	−0.0001(1)	−0.0004(2)	0.0000(1)
Te(3)	0.015(1)	0.0009(1)	0.016(1)	−0.0001(1)	0.0006(1)	−0.0001(1)
Te(4)	0.032(2)	0.0011(1)	0.018(2)	−0.0001(1)	−0.0001(2)	0.0008(1)
Te(5)	0.032(2)	0.0008(1)	0.017(2)	0.0001(1)	−0.0006(1)	−0.0006(1)
Te(6)	0.013(2)	0.0004(1)	0.020(2)	0	0.0002(2)	0
Te(7)	0.011(2)	0.0008(1)	0.018(2)	0	0	0.0002(1)
Te(8)	0.013(1)	0.0009(1)	0.019(1)	0.0000(1)	−0.0001(1)	0.0001(1)
Te(9)	0.015(1)	0.0003(1)	0.022(2)	−0.0001(1)	−0.0005(1)	−0.0001(1)
Te(10)	0.012(1)	0.0013(1)	0.034(2)	0.0000(1)	−0.0001(1)	−0.0001(1)
Te(11)	0.014(1)	0.0013(1)	0.034(2)	0.0000(1)	−0.0002(1)	0.0002(1)
Te(12)	0.016(2)	0.0006(1)	0.039(3)	0	−0.0004(1)	0
Ag(1)	0.026(2)	0.0028(2)	0.015(3)	0	0	0.0003(3)
Ag(2)	0.027(2)	0.0030(2)	0.013(2)	0.0002(2)	0.0001(2)	0.0004(2)
Ag(3)	0.025(2)	0.0023(1)	0.018(2)	−0.0002(2)	0.0001(2)	0.0004(2)
Ag(4)	0.032(2)	0.0030(1)	0.017(2)	−0.0003(2)	−0.0005(2)	0.0004(3)
Ag(5)	0.026(2)	0.0017(1)	0.028(2)	−0.0003(2)	−0.0005(2)	−0.0003(3)
Ag(6)	0.031(3)	0.0019(2)	0.029(3)	0	−0.0002(3)	0
K1/Eu4	0.003(2)[a]					
K2/Eu5	0.002(1)[a]					
K3/Eu6	0.001(1)[a]					

[a] The disordered K/Eu sites were isotropically refined only.

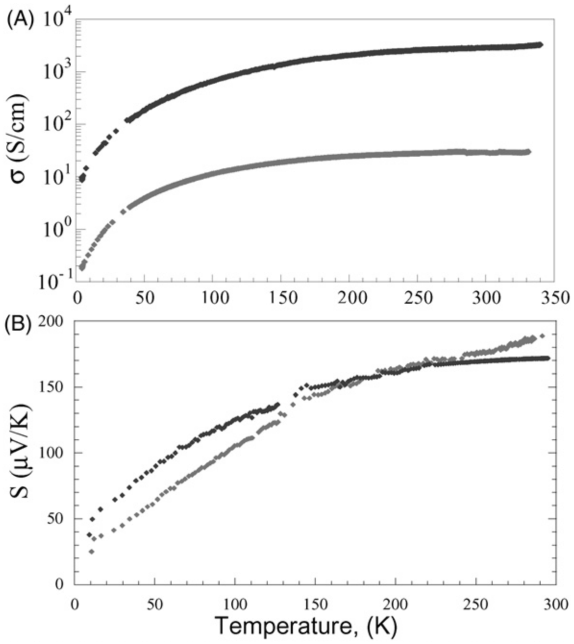

Fig. 20 (A) Four-probe electrical-conductivity data for single crystals of $K_{0.65}Ag_2Eu_{1.35}Te_4$ as a function of temperature. (B) Thermopower data for single crystals of $K_{0.65}Ag_2Eu_{1.35}Te_4$ as a function of temperature.

atom in the net. Interestingly, $KCuCeTe_4$ and KCu_2EuTe_4 possess the same average charge but exhibit different supercells. This is an indication that the modulation is not only affected by the electron count, but also by the remaining part of the structure and its makeup. While we have been able to solve some of these Te net distortions, others remain elusive. Most of these materials were determined to be p-type semiconductors with narrow bandgaps ranging around 0.1–0.3 eV. However, to fully understand the nature of these Te net distortions, further experimental and theoretical work is needed. More of these types of compounds need to be studied to systematically build a relationship between the electron count and the type of distortion. It would appear that these nets are stabilized in compounds with large multiply charged atoms capable of adopting high coordination numbers such as Ba^{2+}, Eu^{2+} and Ln^{3+}. Similar superstructures to those discussed in this paper also exist in selenides. Lee *et al.* have applied second-moment scaled Huckel theory to rationalize or predict superstructures found in elemental selenium, LnQ_2 (Ln = La, La, Ce; Q = S, Se), $Ln_{10}Se_{19}$ (Ln = La, Ce, Pr, Nd, Sm), and $RbDy_3Se_8$.[13] All these structures contain distortions of square lattices of chalcogen atoms. In the case of $Ln_{10}Se_{19}$ and $RbDy_3Se_8$, these lattice distortions are coupled to ordered defects in the chalcogen square lattice. On the basis of energy calculations, Lee *et al.* proposed eight ground state $RbDy_3Se_8$ superstructure patterns among the 5×10^5 possible alternatives. In a fascinating result, the binary phase $DySe_{1.84}$ was shown to posses a 66-fold superstructure deriving from an ordering of polyselenide ions associated with a flat Se net.[27] Finally, we wish to remark that in the future structures that appear to have square chalcogenide nets should be viewed with suspicion and additional evidence for some type of distortion (periodic or even random) should be sought.

Acknowledgement

Financial support from the National Science Foundation is gratefully acknowledged. This work made use of the SEM and TEM facilities of the Center for Advanced Microscopy at Michigan State University.

References

1 R. Patschke, J. Heising, J. Schindler, C. R. Kannewurf and M. G. Kanatzidis, *J. Solid State Chem.*, 1998, **135**, 111.

2 (*a*) X. Zhang, J. L. Schindler, T. Hogan, J. Albritton-Thomas, C. R. Kannewurf and M. G. Kanatzidis, *Angew. Chem. Int. Ed. Engl.*, 1995, **32**, 68; (*b*) K. S. Choi and M. G. Kanatzidis, *J. Solid State Chem.*, 2001, **161**, 17.

3 (*a*) X. Zhang, J. Li, B. Foran, S. Lee, H.-Y. Guo, T. Hogan, C. R. Kannewurf and M. G. Kanatzidis, *J. Am. Chem. Soc.*, 1995, **117**, 10 513; (*b*) The tetragonal structure of $K_{0.33}Ba_{0.67}AgTe_2$, determined by conventional crystallography, is inconsistent with its semiconducting behavior. This is because conventional crystallography gives the average structure, which is a perfect square Te-net

4 (*a*) W. Lin, H. Steinfink and F. Weiss, *J. Inorg. Chem.*, 1965, **4**, 877; (*b*) R. Wang, H. Steinfink and W. F. Bradley, *Inorg. Chem.*, 1966, **5**, 142; (*c*) M.-P. Pardo, J. Flahaut and L. C. R. Domange, *Bull. Soc. Chim. Fr.*, 1964, 3267; (*d*) T. H. Ramsey, H. Steinfink and E. Weiss, *Inorg. Chem.*, 1965, **4**, 1154; (*e*) B. K. Norling and H. Steinfink, *Inorg. Chem.*, 1966, **5**, 1488.

5 M. Wachhold and W. J. Sheldrick, *Angew. Chem. Int. Ed. Engl.*, 1995, **34**, 2109.

6 J. Cody and J. A. Ibers, *Inorg. Chem*, 1996, **35**, 3836.

7 A. C. Sutorik and M. G. Kanatzidis, *Prog. Inorg. Chem.*, 1995, **43**, 151.

8 R. Patschke, J. Heising, P. Brazis, C. R. Kannewurf and M. G. Kanatzidis, *Chem. Mater.*, 1998, **10**, 695.

9 R. Patschke, Ph.D. Dissertation, 1999, Michigan State University.

10 R. Patschke, P. Brazis, C. R. Kannewurf and M. G. Kanatzidis, *J. Mater. Chem.*, 1999, **9**, 2293.

11 B. K. Norling and H. Steinfink, *Inorg. Chem.*, 1966, **5**, 1488.

12 Y. Park, M. G. Kanatzidis, unpublished results.

13 S. Lee and B. Foran, *J. Am. Chem. Soc.*, 1994, **116**, 154.

14 For comprehensive reviews of CDWs, (*a*) *Electronic Properties of Quasi-One-Dimensional Materials*, ed. P. Monceau, Reidel, Dordrecht, 1985; (*b*) G. Gruner, *Rev. Mod. Phys.*, 1988, **60**, 1129; (*c*) Low-Dimensional Electronic Properties of Molybdenum Bronzes and Oxides, ed. C. Schlenker, Kluwer Academic Publishers, 1989; (*d*) *Physics and Chemistry of Low Dimensional Inorganic Conductors*, ed. C. Schlenker and M. Greenblatt, Plenum, New York, 1996; (*e*) For a review of the Peierls transition, see J. P. Pouget and R. Comes, in *Charge Density Waves in Solids*, ed. L. P. Gor'kov and G. Gruner, North Holland, Amsterdam, 1989, p. 85.

15 G. A. Papoian and R. Hoffmann, *Angew. Chem. Int. Ed. Engl.*, 2000, **39**, 2409.

16 E. DiMasi, M. C. Aronson, J. F. Mansfield, B. Foran and S. Lee, *Phys. Rev.*, 1995, **B52**, 404.

17 (*a*) E. DiMasi, M. C. Aronson, J. F. Mansfield, B. Foran and S. Lee, *Phys. Rev. B.*, 1995, **52**, 14 516; (*b*) B. Foran and S. Lee, *J. Am. Chem. Soc.*, 1994, **116**, 154; (*c*) E. DiMasi, B. Foran, M. C. Aronson and S. Lee, *Chem. Mater.*, 1994, **6**, 1867; (*d*) B. Foran, M. C. Aronson, S. Lee and M. C. Anderson, *Chem. Mater.*, 1993, **5**, 974.

18 O. Gourdon, J. Hanko, F. Boucher, V. Petricek, M.-H. Whangbo, M. G. Kanatzidis and M. Evain, *Inorg. Chem.*, 2000, **39**, 1398.

19 D. B. Brown, J. A. Zubieta, P. A. Vella, J. T. Wrobleski, T. Watt, W. E. Hatfield and P. Day, *Inorg. Chem.*, 1980, **19**, 1945.

20 The original data was collected on a Rigaku AFCS four-circle diffractometer, which unfortunately was not sensitive enough to detect such weak supercell reflections. Another crystal was therefore mounted on the more sensitive Siemens SMART Platform CCD diffractometer using graphite monochromatized Mo-Kα radiation. The data were collected over a full sphere of reciprocal space, up to 50° in 2θ. The individual frames were measured with an ω rotation of 0.3° and an acquisition times of 60 s frame^{-1}. The SMART software was used for the data acquisition and SAINT for the data extraction and reduction. The absorption correction was performed using SADABS. The structure was solved by direct methods using the SHELXTL package of crystallographic programs.

21 Another complication, for both compounds, lies in the fact that the crystals were micro-twinned. The morphology of the crystals is that of very thin square plates. This combination allows the crystals to stack and twin very easily, in a merohedral fashion. The crystallographic reflections were therefore overlapping in their positions, leading to an observed electron density much higher than calculated. This results in a poor refinement and significant residual electron density in the Fourier map. Since it seemed impossible to find a truly "single" crystal, attempts were

made to correct for this twinning by applying a twin law to the data. Several twin laws were tried, based on modeling how the "twinned" cell is vectorially related to the original cell. The twin law that gave the best improvement on the refinement was one which the two cells are related by a mirror perpendicular to the *ac* plane: $\begin{bmatrix} a' \\ b' \\ c' \end{bmatrix} = \begin{bmatrix} a \\ b \\ c \end{bmatrix} \cdot \begin{bmatrix} -1 & 0 & 2 \\ 0 & -1 & 0 \\ 0 & 0 & 1 \end{bmatrix}$ By applying this twin law, the R factors ($R/wR2$) in the refinement dropped from 12.09/39.77 to 10.41/32.34. The Flack parameter was also refined, indicating that 42% of the crystal belonged to a fragment defined by this twin law.

22 Since partial occupancy on copper is unusual and the crystals were originally isolated from a Rb_2Te_x flux, careful elemental analysis was performed on the single crystal after data collection was complete. This analysis not only confirmed the absence of rubidium, but verified the copper composition to be exactly 0.66.

23 G. Cordier, H. Schäfer and P. Woll, *Z. Naturforsch.*, 1985, **40b**, 1097.

24 Na^+ and Ag^+ have an ionic radii of 1.02 Å and 1.15 Å, respectively, similar enough to allow the two metals to occupy the same site, which is also square antiprismatic.

25 (*a*) G.-H. Gweon, J. D. Denlinger, J. A. Clack, J. W. Allen, C. G. Olson, E. DiMasi, M. C. Aronson, B. Foran and S. Lee, *Phys. Rev. Lett.*, 1998, **81**, 886; (*b*) E. DiMasi, B. Foran, M. C. Aronson and S. Lee, *Phys Rev. B.*, 1996, **54**, 13 587.

26 Variable temperature magnetic susceptibility data for KCu_2EuTe_4 was measured over the range of 5–300 K at 6000 G. A plot of $1/\chi_m$ *vs.* T shows that this material exhibits perfect Curie–Weiss behavior. A μ_{eff} value of 7.58 BM and a Weiss constant of −75 K was estimated by fitting a straight line to the data above 140 K. Analogous data collected for $Na_{0.2}Ag_{2.8}EuTe_4$ at 3000 G gave a μ_{eff} of 8.59 BM and a Weiss constant of −4 K. These values are consistent with an f^7 configuration or Eu^{2+} (7.9–8.0 BM) and are very different from that expected for Eu^{3+} (3.3–3.5 BM).

27 S. Lee and B. Foran, *J Am. Chem. Soc.*, 1996, **118**, 9139.